Theorem

definition Definition

DEVELOPMENT OF FAR-IR ULTRAFAST TIME-RESOLVED AND POLARIZATION DEPENDENT TECHNIQUES FOR INVESTIGATION THE CHARGE CARRIERS DYNAMICS IN TOPOLOGICAL INSULATORS.

by

DLER KAREEM

A thesis submitted to
The University of Birmingham
for the degree of
DOCTOR OF PHILOSOPHY

Nanoscale Research Group
College of Engineering and Physical Sciences
The University of Birmingham
December 2023

Abstract

This thesis investigates the ultrafast dynamics of photo-excited carriers on the surface of a topological insulator sample Bi_2Te_3. The work involves two parts. The first part of this work describes the use of time resolved spectroscopy as a technique with an infrared probe being used in conjunction with a visible pump. An ultrafast laser system was employed in this work and shows the advantage of using an infrared probe to investigate the dynamics of free carriers on the surface.

We studied the reflectance of the probe with different pump power and different probe polarization states. It was found that reflectance signals indicated the surface plasma wave generated by a visible pump that excited the surface. A surprising finding is that the decay time of the surface wave increases as pump fluence increases. The results showed that Bi_2Te_3 can be employed for high-speed switching in infrared devices and optical communication.

The second part of this work is devoted to the development and application of the time resolved ellipsometry method to investigate how the refractive index of the topological insulator surface evolves in time. We developed an ellipsometry set-up by using a visible pump and an infrared probe. We have demonstrated how the complex refractive index changed following excitation. The results indicate that the refractive index reduced after excitation, while the extinction coefficient increased. In addition, the complex refractive index is recovered in a few picoseconds. From our results, we suggest that, by combining ultrafast surface plasma generated on the metallic surfaces with highly tunable refractive index in the infrared region, Bi_2Te_3 thin films can be used efficiently in optical devices for light control.

ACKNOWLEDGEMENTS

First and foremost, I would like to thank my mother and all members of my family for their support.

It is also my honor and pleasure to thank my supervisor, Dr. Andrey Kaplan, for his support and for his professional guidance and supervision. Throughout my PhD research, he has always been a reliable source of support for me. This thesis would not have been possible without the consistent encouragement of my supervisor Andrey Kaplan.

Aside from that, I would like to thank Dr. Rihan and Dr. Jack for their help in the lab. Both of them were very helpful to me. Also I would like to thank Dr. Amar for his help.

Additionally, I would like to thank my friend in the nanoscale physics group Dr. Gazi Aliev for his help.

I also want to thank everyone in the group for letting me have a good time despite the hard work. I would like to conclude by thanking the Ministry of Higher Education in Iraq for providing me with the opportunity to study for my Ph.D. at the University of Birmingham.

CONTENTS

CHAPTER 1

INTRODUCTION

Over the past two centuries, physicists have tried to understand why electricity flows through some materials instead of others. Benjamin Franklin Around the mid-17th century was the first to come up with the concept that electricity had negative and positive elements and that electricity flowed between these elements. Additionally, he believed that lightning was a form of this flowing electricity [1]. As early as the 18th century, some experiments were undertaken to understand conductivity. An autodidactic British scientist Gray, observed that certain materials conduct electricity [2], while others, such as silk or wool, do not. The discovery of quantum physics in the 20th century presented scientists with new tools to investigate electron properties.

According to the band theory materials can be grouped into three types, insulators, conductors, and semiconductors. Band gap is the main factor in this classification. In conductors, the conduction bands and the valence bands are not separated, the energy gap thus does not exist. There is partially occupied conduction band (even at low temperatures), resulting in a high electrical conductivity. Thus there are no restrictions to prevent freedom of carriers movement in conductors materials.

In insulators, there is a wide band gap between the conduction and valence bands. The band gap prevents electrons from gaining access to the conduction band. Semiconductors have a small gap, so if the electrons are sufficiently energetic, they can populate into the conduction band.

In recent years, a new type of material called topological insulators(TI) has been discovered. The topological insulator, a relatively novel concept in condensed matter physics and is growing in importance. TI manipulates electricity in a unique manner. Topological insulators conduct no current in their bulk, just like conventional insulators. In contrast, a material acts like a conducting material near the edges (in the case of 2D materials) or on the surface (for 3D materials). Due to the fact that TIs have a characteristic electronic structure which induces spin coupling. As a result, they have unique properties due to exclusive symmetry. The current will not be disrupted or rerouted by small imperfections or changes on the surface. The importance of TI goes beyond its fundamental significance in the condensed matter field because it could be applied to future technology.

It is important to note that the research into topological conductivity was developed through a series of steps in this field.

1.1 Review of Topological Insulators

In 1980, the Quantum Hall effect was discovered by Klitzing et.al.[3], when they measured the Hall voltage of two-dimensional electronic gas and they determined that the degenerate electron gas is completely quantized at liquid helium temperature and an intense magnetic field of order 15 T [3]. This discovery led to the first prediction of TI. In 1982 by Thouless et.al[4] at the University of Washington predicted currents on the edges of two-dimensional materials in the presence of a magnetic field. The genius method was developed by Haldane at the University of California, San Diego in 1988 [5], to achieve the Quantum Hall State (QHS) in solid state materials without applying a magnetic field. Haldane's honeycomb lattice model consists of two pedestals on each side of a graphene-like structure. For the first time, Shuichi and Naoto demonstrated in 2003 that electrons can conduct on insulating surfaces without applying magnetic fields. This phenomenon is known as Quantum Spin Hall effect [6]. In 2005, C. L. Kane and E. J. Mele [7] were able to take another important step forward in order to achieve Haldanes goal. They proved

that spin-orbit coupling, which is a fundamental property in any material, can successfully take place of the magnetic field in Haldanes model. However, it is pertinent to note that the quantum Hall state differs from spin coupling states in that the time reversal symmetry of the quantum Hall state is not preserved. According to Kane and Mele, the electrons in this graphene-like model are in another kind of quantum state which differs from the conventional quantum state. The electrons in this state behave in exactly the same way as they behave in QHE, meaning that, in the bulk, they are insulating, but at the edges, are conducting. In 2007 Liang Fu et. al [8] from University of Pennsylvania generalized the two dimensions quantum spin Hall effect (QSH) states to three dimensions system. In the same year, J. E. Moore and L. Balents [8] at the University of California were the first to coin the term "topological insulator." In 2009, Robert J. and his team at Princeton University observed a three-dimensional topological insulator with properties that could be manifested at near the room temperature [9].

1.2 Motivation

Two primary factors make TI material an appealing topic, first, its unique properties and second, the fact that it can be found naturally, meaning it does not require manufacturing. The topological insulator, a relatively new concept in condensed matter physics, is growing in importance. The discovery of TI has significant implications for basic physics and semiconductor devices. This material has Quantum Spin Hall states (QSH) at room temperature without applying a magnetic field, which gives it engineering and application value. Most studies of TI, however, attempt to demonstrate the superior nature of TI and subsequently employ it in practical engineering and application.

Since the properties of TI are tied to the structure, it is possible to slice it and the pieces retain the unique properties of the crystal. The study of topological insulators and their applications is equally critical as understanding their topological properties. Many applications are based on the properties of TI, such as semiconductor and optoelectronic

devices, magnetic devices, lasers, and photodetectors based on TI. For any application to succeed, TI capabilities must be fully understood. It is important to understand, for example, if TI used in photodetectors, some parameters of response time (rise time, fall time) and responsivity should be investigated and understood. For transistors based on TI, it is necessary to study the carriers dynamics in the conduction band and the surface states. There are a variety of factors that affect the optical properties of the surface of the TI, and understanding all of these factors is necessary for the development of any optical device based on TI. The aim of our study is to investigate the electro-optical properties of the surface state and to observe the ultrafast dynamics of the carriers in the surface states. Few studies have been conducted using a visible pump and an infrared probe to investigate the optical properties of TI, as the plurality of the studies used pump and prob in the visible region [10, 11].

There are different ways to investigate the electro-optical properties of the surface of any sample. In order to study the dynamics of free carriers on the surface of the sample, a pump probe technique can be used effectively. An investigation of optical and acoustic phonons as well as the recombination time of free carriers was conducted using visible pump and visible probe measurements. [12, 10, 13, 14, 15].

The purpose of this work is to investigate the free carriers on the surface of TI using two different techniques. The first technique is time-resolved spectroscopy, while the second is time-resolved ellipsometry. Both experiments were conducted using a visible pump and an infrared probe. The use of an infrared probe offers some advantages in time-resolved spectroscopy measurements. For example, it is possible to avoid interband excitation by using a probe in IR energy, in which case only free carriers will be detected on the sample's surface. In addition to detecting the plasma generated on the surface of semiconductors, an IR probe is more appropriate since the plasma frequency is located in the IR region.

On the other hand, the ellipsometry technique is an effective method for determining the dielectric properties of thin films or bulk materials. Developing time-resolved

ellipsometry setups is intended to determine how refractive index changes as a result of excitation of free carriers on the surface. However, this could be the first work investigating the electro-optical properties of TI using time-resolved ellipsometry using visible pump and IR probe. Using IR probe in time resolved ellipsometery could be difficult to alignment, this could be the reason why there is no such works in the literature.

This thesis is organized in the following way: The characteristics and methods used to understand the electronic structure and the carrier properties were discussed in chapter 2. This is followed by a description of several of the physical phenomena that have led to the emergence of TI as a result of these phenomena. Chapter 3 focused on the structure properties of own sample and the description of the femtosecond laser system that was employed in this experimental work. Then, time resolved spectroscopy is discussed with the background theory, the excitation, reflection and relaxation processes related to the pump probe technique were presented in details. In chapter 4, The results and discussion of the time-resolved measurements were presented. In Chapter 5, time-resolved ellepsometry is described using an infrared probe, along with the results and discussion of the measurements.

CHAPTER 2

FUNDAMENTAL PRINCIPLES OF TOPOLOGICAL INSULATORS

2.1 Topological Insulators (TI)

The electronic states and the fundamental properties of TI have been studied using a variety of techniques, for example, Scanning Tunneling Microscopy (STM)[16, 17, 18, 19] By employing this technique, it is possible to obtain a profile of the surface in three dimensions. By using this method, it is possible to determine surface roughness, detect defects on the surface, and determine the conformation of molecules and particles on the surface.

Another method for studying the properties of TI is by using Angle-resolved Photoemission Spectroscopy (ARPES). [20, 21, 9] It is possible to determine the energy and momenta of electrons within a material using this technique. Furthermore, the transport measurements technique can be used to study the emerging quantum properties of TI [22, 23, 24, 15]..

On the other hand, the time-resolved pump probe technique is the most widely used method for studying the electro-optical properties and dynamics of free carriers. The objective of this study is to investigate the electro-optical properties of TI samples using time-resolved spectroscopy and time-resolved ellipsometry.

The dynamics of electrons and phonons, such as their excitation and relaxation pro-

cesses, occur on time scales ranging from femtoseconds to picoseconds[25]. In order to observe ultrafast events, the time resolution of the experimental setup must be shorter or in the same range as that of the events being investigated. It has been possible to observe these ultrafast processes since the mid-20th century as a result of the development of ultrafast lasers. According to Einstein's theory in 1916 corresponding photons generating coherent light could be produced via the process of stimulated emission. Following that, development of Q-switching and mode-locking technologies gave rise to the capability to produce ultrafast laser pulses within the femtosecond timescale, which enabled the observation ultrafast dynamic processes[26, 27]. This work particularly emphasizes on the developing tools and probing the carrier dynamics of the surface of TI. Bi_2Te_3 has been chosen as a TI sample in this study due to its importance for developing TI-based device applications [22]. Accordingly, researchers have concentrated their efforts on investigating the electronic and optical properties of Bi_2Te_3 recently. Specifically, time-resolved spectroscopy was intensively employed to investigate the transport and dynamics properties of the hot carriers in TI. In order to determine a material's suitability for a particular application, it is essential to firstly understand the free carrier behavior of the material. As an example, sensors and transistors are designed to operate at high performance levels, so carriers must travel to the electrodes before they can be recombined[28, 29, 30] However, in contrast to that, fast recombination and rapid electron-hole relaxation are required for applications such as switches [31, 32, 33].

The majority of studies investigating the electro-optical properties of TI have been conducted using visible pump and visible probe technique[10, 11].

Optical and acoustic phonons have been investigated using a visible pump and visible probe [34]; in addition, the scattering of the hot carriers and relaxation time have also been examined using a visible probe [35].

A study of the optical properties of topological insulators materials in the infrared region may provide information that can be used for the development of optical devices. An example would be devices based on the interaction between infrared light and matter,

such as mid-IR detectors and IR sensors.

In this work, ultrafast lasers that are capable of providing pulses with a time duration of less than 80 femtoseconds have been used in order to investigate the electro-optical properties of the surface of the TI sample. This work aims to investigate the electro-optical properties of the free carriers on the surface of TI samples using time resolved spectroscopy and time resolved ellipsometry, which is accomplished by building an ellipsometry set-up. The novel aspect of this work is that it employs a 4 μm probe to investigate free carriers in a pump probe technique. The time-resolved ellipsometry with the IR probe is rarely used in the literature for the study of TI.

2.2 Hall Effect

Hall effect occurs when magnetic fields applied perpendicularly to currents flowing through conductors result in voltage differences across the conductors [36]. The generated voltage (Hall voltage) is transverse to the current and the magnetic field [37]. The Hall effect arises as a result of the characteristics of the current flowing through a conductor. There are many small carriers of charge that make up current, including electrons, holes, ions, or a combination of these carriers. In the presence of a magnetic field, the charges are subjected to a force, which is known as the Lorentz force [38]. In the absence of such a magnetic field, charges tend to travel in straight lines when they collide with impurities, phonons, and other particles. A perpendicular magnetic field causes the carriers to follow curved paths, resulting in moving charges accumulating on one surface of the material. This results in opposite and equal charges appearing on the other side, where mobile charges are scarce. As a result, there is an asymmetric concentration of charge density within the Hall element. This is occurring due to a force which is perpendicular to both the magnetic field and the straight path. Separation of charges creates an electric field which prevents further charge migration, and a steady electric potential is maintained while the charge is flowing. Figure 2.1 shows the Hall effect (HE), where the electronic

current flows along the conductor, causing the Hall voltage which depends on the applied magnetic field (B) and the current (I)

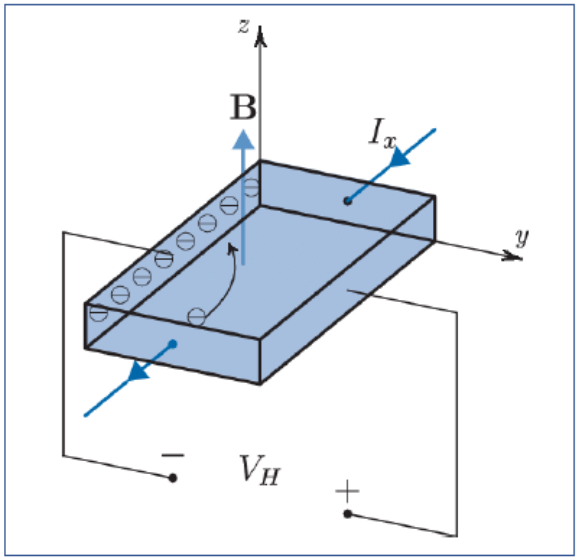

Figure 2.1: The Hall effect occurs in a conductor, where B is the applied magnetic field, I is the current and V_H Hall voltage.

The Hal voltage V_H can be expressed as follows [37]:

$$V_H = \frac{IB}{qnd} \tag{2.1}$$

Here,I is the flowing current, B is the strength of the magnetic field, q represents a charge, n is the carriers number per unit volume and d is the thickness.

Accordingly, the Hall coefficient , defined as the ratio of the induced electric field by the external magnetic field to the current density generated, can be expressed as follows.

$$R_H = E/jB \tag{2.2}$$

Where R_H represents the Hall coefficient, j represents the current density of the carriers, E represents the induced electric field, and B represents the magnetic strength.

2.3 Quantum Hall Effect

The quantum Hall effect refers to a quantized version of the Hall effect. This phenomenon occurs when a two-dimensional electron system is placed under conditions of a strong magnetic field and a low temperature. In this situation, the Hall resistance displays a quantized value. This effect was first observed in 1980 by von Klitzing et al.[39]. It had been found that quantum Hall conductance should be quantized and highly precise. The mathematical formula to describe the Quantum Hall effect can be expressed as follows [40]:

$$\alpha = I/V_H = ve^2/h \tag{2.3}$$

α is the Hall conductance, I is the current, V_H is the Hall voltage, e is the element charge, v is the filling factor and h is Plank constant. The filling factor values can either be an integer value or a fractional value. Figure 2.2 shows the Quantum Hall Conductance (QHC) as a function of the applied magnetic field.

The quantized phenomenon of quantum Hall effect results from the fact that electrons can only exist in certain orbits due to their wave properties. When the magnetic field increases, the electron orbit is changed. The electrons can not move to a new orbit until the field hits them to move to a new orbit. The conductance should takes a certain value and stay at the value as the field increased until the next resonance when the conductance makes a rapid jump to a different value. The value of the quantum Hall conductance does not depend on the purity or geometry of a sample [41].

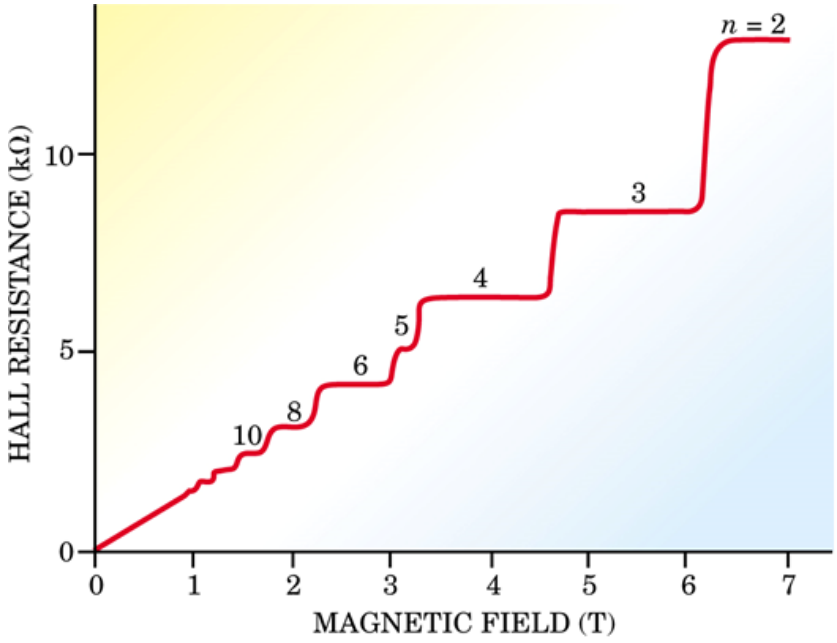

Figure 2.2: Quantum Hall effect in two dimensions semiconductor at low temperature . the series steps represent the Hall resistance as a function of the applied magnetic field [42] .

2.4 Quantum Spin Hall Effect

Quantum Spin Hall effect (QSH) represents the phenomena of creating surface states on the surface of material without applying external magnetic field First evidence suggesting the existence of a quantum spin Hall state was presented in 2005 by Charles Kane and Gene Mele[7] as an adaptation of an earlier model for graphene by M. Haldane[43] that exhibits an integer quantum Hall effect. In 2006 Zhang et al. developed a theory method predicting QSH effect in quantum wells made of Mercury Telluride [44]. In 2007 Molenkamp et al. created the recommended wells and experimentally confirmed of exsiting of QSH effect not in graphene but in mercury telluride quantum wells [45].

Quantum spin Hall effect QSH is the phenomenon which explains how the TI materials have surface states in their edges. Instead of external magnetic field, spin coupling takes place of the external magnetic field. The interaction between the spin angular momentum of the electron and their orbital angular momentum in the atoms pushes the energy levels

up and down in a way that creates a spin-dependent surface state. This spin-orbit be stronger for heavier atoms. In the QSH state there are two edge states instead of just the one in the quantum Hall state. The two edges have opposite spin directions, one spins up and the other spins down. Figure 2.3 shows QSH system where two QH system are combined and each of them has opposite spin direction one is up and another is down. Where in QH there is one edge state while there are two edge states in QSH.

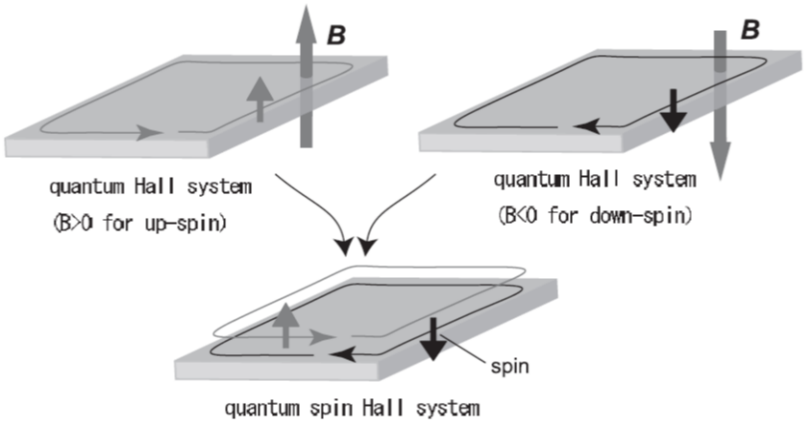

Figure 2.3: Schematic representation of two quantum Hall systems with opposite directions and a quantum spin Hall system resulting in a superposition of those two quantum Hall systems [46].

To better understand Figure 2.4 shows the comparison between insulating, QH, and QSH. Where the red dots represent the applied magnetic field and the arrows circles represent the spin.

According to our previous discussion, QSHE plays a key role in the formation of topological phases in heavy atomic number materials when the materials match certain conditions.

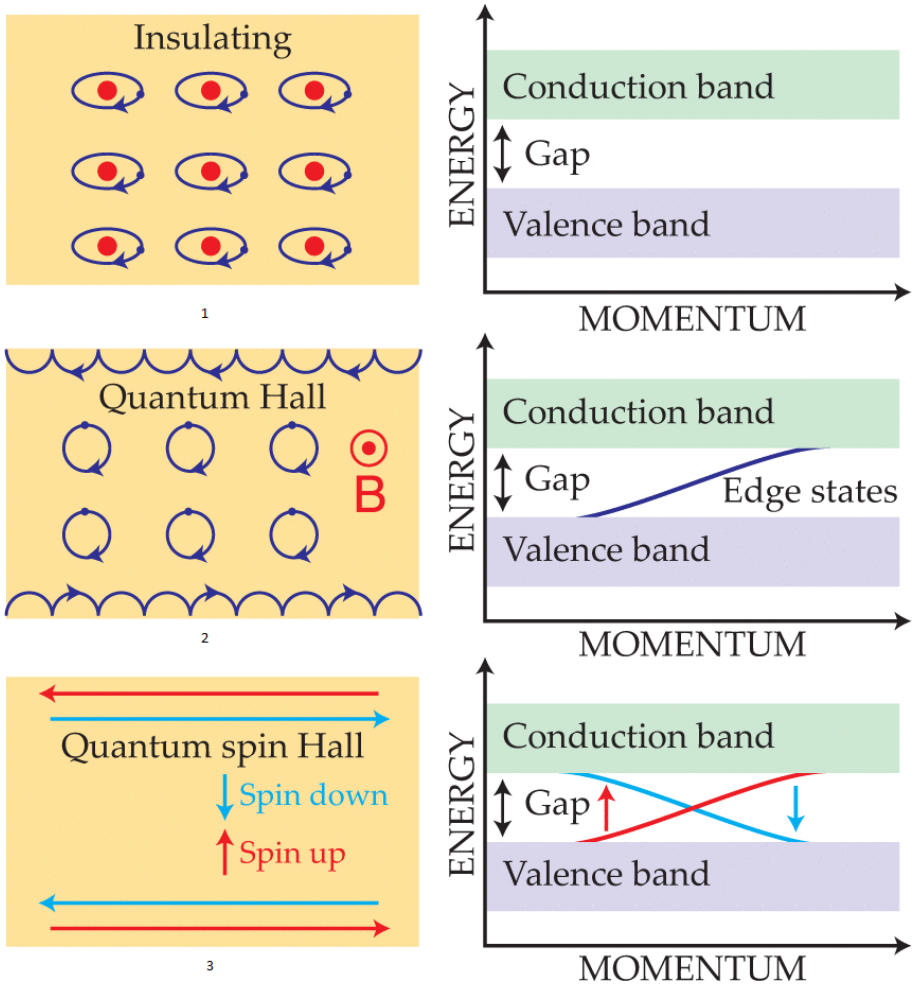

Figure 2.4: The figure shows three band structures, insulator(1), quantum Hall structure(2) and quantum spin Hall regime(3). In insulators the electrons are bound by the atoms. The magnetic field pinning the outer electrons creates the gap in the quantum Hall system that is responsible for carrying current across the edge states. In the quantum spin hall regime there are tow edge states carrying spin-up and spin-down electrons crossing the band gab [47]

In order to demonstrate the unique properties of TIs, it is necessary to present the above phenomena (Hall effect, Quantum Hall effect, and Quantum Spin Hall effect) to the viewer in order to understand why TIs possess these unique properties. In a nutshell, for a material to have free electrons on its surface, it must possess a force that propels the electrons from the bulk to the surface. It can be accomplished by applying a magnetic field normal to the surface of a material that contains electrons in motion. Spin orbit coupling takes the place of a magnetic field, however, the spin of electrons is correlated

with the direction of motion, and electrons move upward or downward depending on their spin direction [48]. In topological insulators, electrons on the material surface are locked to the orientation of electron spins.

2.5 Topological Invariant Z_2

Topological invariance can be defined simply as the gapless state that appears as an electronic state at the boundary of the sample.

The stability of an edge state in a quantum spin Hall state is determined by the level of a particular point between the two bands (valence and conduction bands), where the two edges branch cross each other at zero momentum, as illustrated in Figure 1.5. In this case the level of crossing point at k=0 is protected by the time reversal symmetry which flips the momentum and spin of the electrons. The electrons in two edge states in opposite momenta k and +k behave such as a Karmers pair in time reversal symmetry, when the energy level of each particle degenerate with time reversal for its partner[41]. The edge states in two-dimensional topological insulators could help to understand the topological invariant. In the Figure 2.5 half of the Brillouin zone is shown to illustrate the way that both valance and conduction bands connect to each other.

The half of Brillouin zone is shown because of the other half is a mirror of it. From the figure it is clear there are two types of edge states in two dimensions to connect the valance and conduction bands; where Γ_a=0 $< k_x < \Gamma_b = \pi/2$. In the QSH state, the edge is robust and crosses the Fermi level with an odd number, such as in case (b). While in case (a), the edge state can be eliminated and it crosses Fermi level in an even number; this type of edge is in normal insulators. The type of edge state determines the type of time reversal invariant; this explains the origin of topological invariant Z_2 [49].

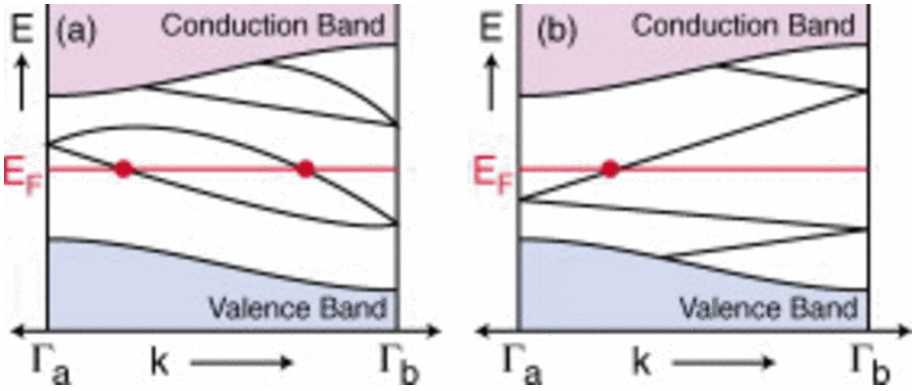

Figure 2.5: Diagram illustrating a half of the Brillouin zone in two-dimensional crystal; it shows the bulk band gaps and edge states as a function of momentum. The edge states at momentum equal to 0 and $\pi/2$ could be connected by only two possible ways which are shown in case (a)the surface state crosses the Fermi level two times; edges are not robust and vanish, such as in ordinary insulators; In the case (b)represents the robust edge states in quantum spin Hall effect, whereby the surface states cross the Fermi level in an odd number; these edge states are created by time reversal symmetry [50].

CHAPTER 3

EXPERIMENTAL METHODS AND THEORY

3.1 Properties of Bismuth Telluride

This study has been conducted to investigate electro-optical properties of the surface of the TI material utilizing the pump-probe technique and time-resolved ellipsometry. For this study, Bismuth Telluride Bi_2Te_3 has been used as a sample of a topological insulator because its topological properties change with thin thicknesses [51]. The spin orbit coupling effect is more pronounced when the thickness is reduced. As the thickness of Bi_2Te_3 is reduced, a conduction surface states develops on the surface, while the bulk is insulating [52]. Bulk Bismuth Telluride is a semiconductor characterized by an indirect band gap 0.15 eV at room temperature. With a thin thickness, this band gap can be reduced to 0.3 eV [53]. The melting point of Bi_2Te_3 is 585 ^0C, and its density is 7.8587 g/cm^3 [54]. It was found that Bi_2Te_3 has a high value of electrical conductivity of $1.1 \times 10^5 Sm/m^2$ and a low thermal conductivity of 1.20 W/(mK) [55]. Recently, studies have attempted improving the efficiency of the topological properties of materials based on Bi_2Te_3 through the development of structures in which the dimensions are reduced. This includes thin films or nanowires [56, 57]

On the other hand, Bi_2Te_3 has been the subject of considerable research because it is a part of a newly discovered group of materials named three-dimensional topological insulators [20]. Subsequently, spin polarized surface current with high-mobility can be

generated in absence of external magnetic fields, leading potentially to new applications in quantum computing or spintronic[58, 59, 60].

In general, the crystal structure of Bismuth Telluride consists of five layers of atoms formed in a hexagonal lattice as shows in Figure 3.1. The layers built in alternative form in the following arrangement : Te(1)-Bi-Te(2)-Bi-Te(1).

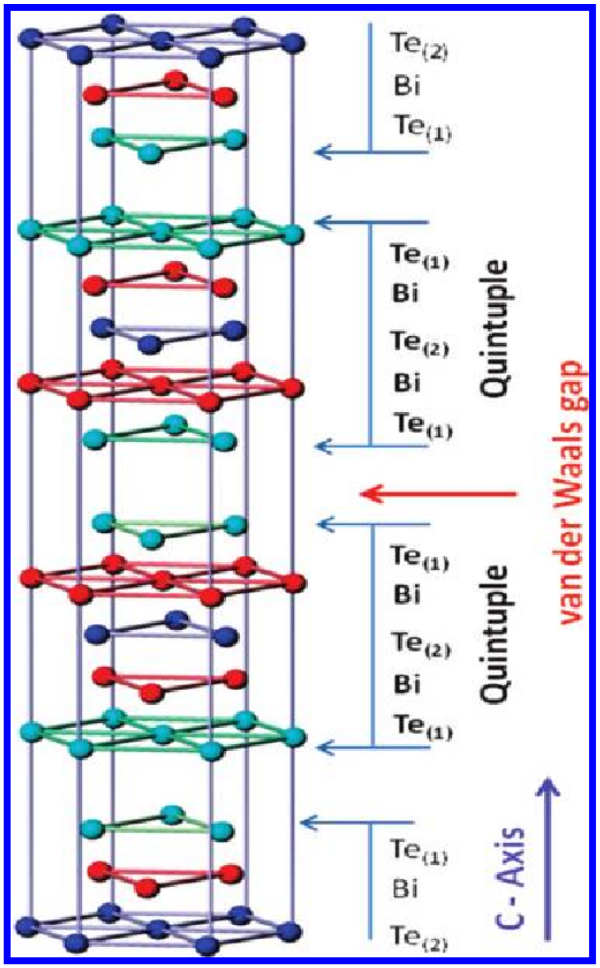

Figure 3.1: Schematic illustration of the atomic structure of Bismuth Telluride and the types of bonds between atoms in the component [61].

The first bond in the structure Te(1)-Bi has three Te(1) atoms neighbours and there are other three Te(2) atoms closest neighbour in sandwich form with Te(2)-Bi. Both Bismuth and Telluride atoms layers in the structure are connected via strong bonds called covalent-ionic bond. , while the bonds between the atoms which is neighbour Te(1) layers is van

der Waals bonds , which is weak.

Due to this reason the Bismuth Telluride crystals can be very easy to be cleaved in perpendicular direction to the trigonal axis . According to the literature, the bulk Bismuth Telluride has an indirect energy band gap, however, valus of energy gap may vary from 0.13 to 0.21 eV [62].

Bismuth Telluride has been shown to have two conductions bands and two valence bands based on studies of its energy band structure. It was suggested that the mechanism behind this doubling was due to overlapping of impurity bands [63, 64].

3.2 Sample Preparation

In order to investigate the optical properties of TI, we prepared the sample in such a way that topological properties are created on the surface of the sample. Since the electronic structure and optical properties of Bi_2Te_3 depend on thickness, surface states can be induced on the surface of the sample when the thickness is decreased [51].

Once the thickness of the crystal is reduced, it becomes a thin-sized crystallite. The electrons in the crystallites will be confined in this small volume, resulting in quantization of electron levels in the conduction band and hole levels in the valence band. As the crystallite size decreases, the band edges will shift far from each other, causing an increase in the energy gap.

There are different ways to prepare samples for induced topological properties of Bi_2Te_3. In this work we used undoped single crystal of Bi_2Te_3 from Hq graphene company. In the literature, TI studies have been used one of the following methods to prepare samples: samples can be grown via the Bridgeman method [65], self-flux method [12], pulsed laser deposition (PLD)[66], molecule beam epitaxy (MBE) [67], chemical vapor deposition (CVD) [68] and mechanical exfoliation method [61]. A piece of Scotch tape was applied on very clean surface of the bulk Bi_2Te_3 sample as shown in Figure 3.2. The sample is high quality undoped crystal from Hq-graphene company. A thin layer of the

exfoliated sample was then placed on a silicon substrate. The exfoliation method was used in this work because the crystal structure of Bi_2Te_3 is easy to cleave as mentioned earlier.

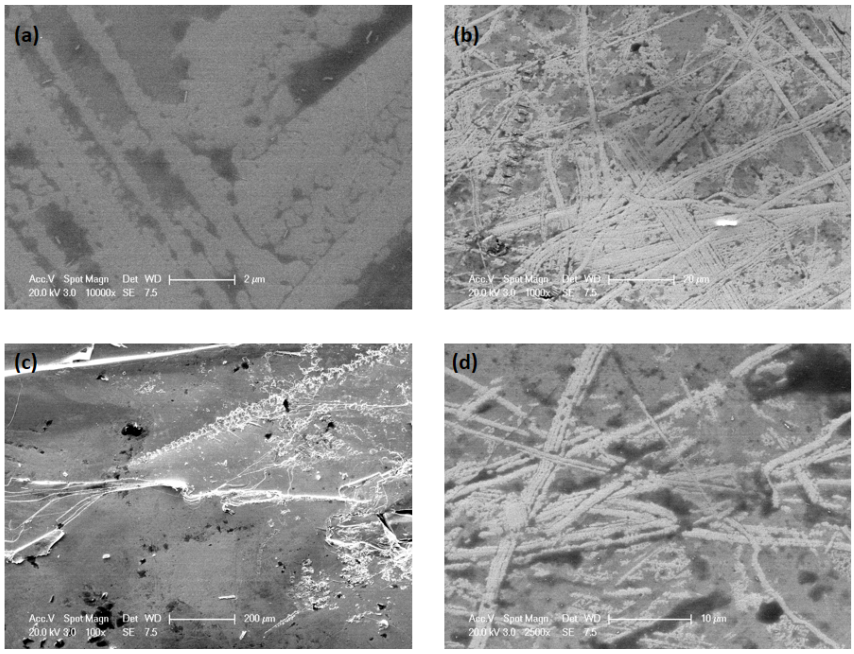

Figure 3.2: Image of the sample surface using SEM with different resolutions:(a) 2 μm (b) 20 μm (c) 200 μm (d) 10 μm.

The weak Vander Waal bond with a length of about 0.37 nm between $T^{(1)} - T^{(1)}$ made mechanical exfoliation a suitable technique to cleave quintuple layers of Bi_2Te_3 crystal. This method is the easiest and most cost-effective way to induce a thin layer of Bi_2Te_3 with topological properties on the surface. In addition, this method provides a high level of structural quality and is more than 100 μm^2 in size [69].

3.3 Femtosecond Laser

Characterization and analysis by optical methods provide advantages such as non-contact, no-damage, fast processing, as well as high accuracy when compared to mechanical and electronic counterparts while in ARPES the electronic state is destroyed. Consequently,

they are widely employed to characterise and investigate different types of materials. For example, through measuring the reflectance and transmittance of a material, it is possible to determine its absorption coefficient, estimate the conductivity, complex permittivity [70] and obtain the band-gap energy [71]. Techniques that are more complicated, for example Raman Spectroscopy and ellipsometry, can further enhance the capabilities of reflection and transmission measurements to study the characteristics of complex structures materials (for example, multilayers) or biological/chemical interactions. Additionally, the properties of the material when excited and the dynamics of the carrier can be determined by enhancing electron transitions to states with higher energy and measuring the temporal variation of reflectance and transmittance [72]. Because these processes have a short lifetime, it is required to use laser with pulse duration faster than the evolution of states.

To study the electro-optical properties and the dynamics of the free carriers on the surface of TI, the ultrafast pump-probe technique has been utilised. In this experiment, we use a femtosecond laser system (Coherent Ltd), consisting of three main components. The first component is a Micra which is a mode-locked seed laser with a central wavelength of 800 nm (CWL) and the full-width at half-maximum (FWHM) is 100 nm. The second part is Regen which is a Q-switch amplifier. The function of the Regen is to amplify 450 mW seed laser to 3 W intense laser with same wavelength and 60 fs pulse duration. The third element is an Optical Parameter Amplifier (Opera) which is converts the Regen laser pulse to tunable output wavelengths ranging from 250 nm to 10μm. Figure 3.3 illustrates the main components of the femtosecond laser.

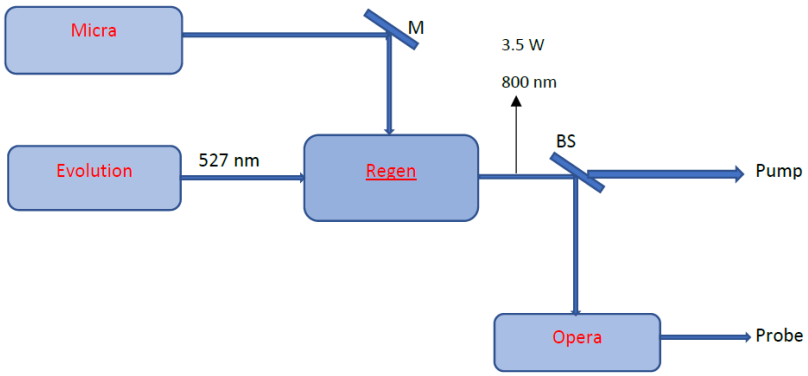

Figure 3.3: A femtosecond laser is composed of three main components: Micra, Regen, and Opera.

Mode-locking and Q-switching will be discussed in the following sections. These techniques are used to produce the seed pulse in Micra and induce ultrafast pulses in Regen. Additionally, the working concept of OPA utilizing optical nonlinearity is discussed.

3.4 Femtosecond Laser Core Techniques

A laser pulse with an extremely short duration can be produced using mode-locking and Q-switching techniques [73]. An essential difference between the two methods is the higher repetition rate and lower power of a mode-locked laser compared to Q-switching. Consequently, a mode-locked laser is mostly utilized as a seed laser for a femtosecond laser, which is then amplified by a Q-switched cavity.

3.4.1 Mode-Locking

The mode locking technique generates an extremely short laser pulse. Photon frequencies in a laser pulse cannot be identical. As a result, they exhibit a Gaussian-like spectrum. The central wavelength and bandwidth of a laser are influenced mainly by the gain medium material [74]. In this work, the gain medium of Regen and Micra is a titanium-doped sapphire crystal (Ti: sapphire) with a 100 nm broad spectrum that can generate pulses

around 800 nm FWHM [75]. Figure 3.4 summarizes and demonstrates the concept of a mode-locked laser. As shown in Figure 3.4(a), the frequency envelope represents the spectrum from a gain medium. The distinct line in the envelope represents the frequencies that correspond to the condition of the standing wave in the cavity $f = cq/2L$, where c is the speed of light, L is the length of the cavity, and q is the mode order. An interference between different frequencies standing waves which results in separate packets of waves with short duration pulses as illustrated in Figure 3.4(b). In contrast to other resonators, a laser with mode-locking has a single-mode output as a result of the mode competition within the cavity. This means that different modes are amplified differently by the same gain medium. The mode which has the highest gain factor dominates all other modes to reach states with stable gain saturation [76].

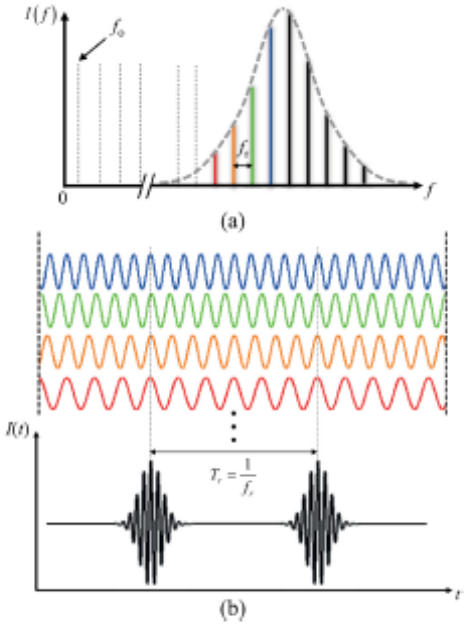

Figure 3.4: Modes of laser (a) in the frequency domains (b) in the time domains [77].

There are two types of mode-locking methods in lasers. The active method and the passive method. Typically, active methods involve modulating the intracavity light with an external signal. Passive methods rely on the self-modulation of laser light caused by

placing some element in the laser cavity in place of an external signal. The mode-locking mechanism in our laser system is passive.

3.4.2 Q-switching

Q-switching is achieved via trapping a laser pulse with a cavity for multiple times to produce multi-stage amplification and generating high power pulses after saturation is achieved. In general, Q-switching technique is divided into two types active and passive.

In active Q-switching laser pulses are triggered by external output triggers, such as mechanical shutters, electro-optical modulators, or acousto-optical modulators. In our femtosecond laser system, two pockel cells were used to trap and output pulses by changing the polarisation of the beam inside the cavity. The s-polarised seed beam is coupled to the Q-switch cavity by mirror RM7 (Figure 3.5). The wave passes twice through the quarter-wave plate RWP , causing the polarisation to change from s to p, then after one round trip leaves the cavity via reflection from the output coupler RP. By switching on the first pockel cell (PC1), it changes the pulse polarization as a quarter-wave plate, thus cancelling the change in polarization caused by the RWP. At this stage the beam has remained s-polarised and is trapped within the cavity. The beam undergoes several amplifications before the second pockel cell (PC2) is triggered. S-polarised light is then converted to p-polarised light to leave the cavity [78]

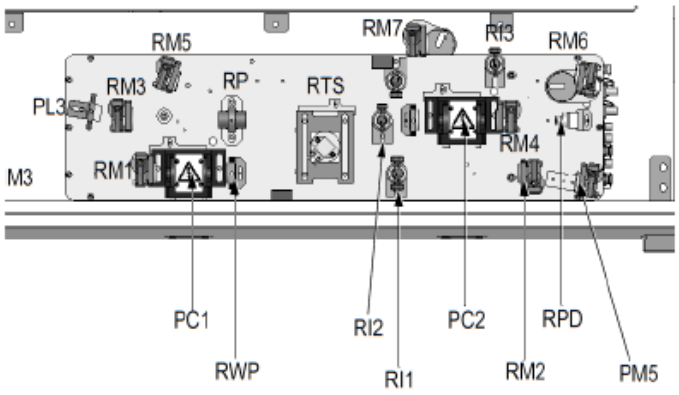

Figure 3.5: An illustration of the cavity of an active Q-switch. RTS is the crystal of Ti-sapphire which is the gain medium; (RM1-4) represtn mirrors form the cavity of amplification; RWP represents a quarter-wave plate, PC1 and PC2 are pockel cells; RP is the output coupler; mirrors RM5-7 are employed to guide the amplified beam to output; RPD represents a fast diode for monitoring the seed beam accumulation [79] .

Passive Q-switching, on the other hand, uses another technique to induce high intense pulses. Q-switching is performed by inserting some kind of variable attenuator within the laser's cavity. The saturable absorber material might be a doped crystal such as Cr:YAG, that is used in Nd:YAG laser Q-switching. Every time the pulse passes through the gain medium, it is trapped in the cavity and amplified. After a number of round trips, the pulse intensity reaches a saturation point, resulting in a significant reduction in adsorption and a significant increase in transmission. A high-power pulse is then emitted from the cavity after passing through the absorber. After that, the absorber returns to a high absorption level due to the low intensity level in the cavity [80]. A passive Q-switching laser with saturable absorbing material is shown in Figure 3.6.

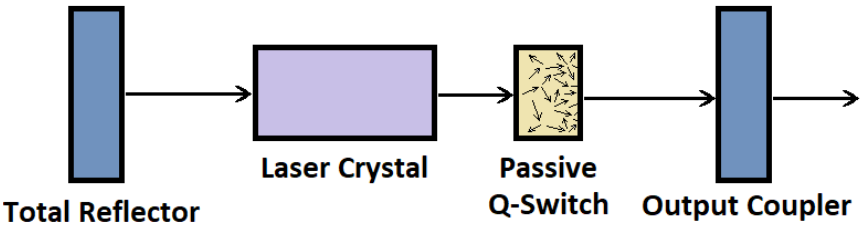

Figure 3.6: Passive Q-switching laser system.

3.4.3 Pulse Amplifcation

This part is divided into three stages. The first step is to provide the seed pulses into stretcher unit to increase the time width of pulses to avoid breakdown of the optics when the pulses are amplified inside the generator. The second stage in the generator takes place when the stretched seed pulses are amplified via another Q-switched Nd:YLF laser with 527 nm wavelength which is produced by evolution. In this stage the average power of amplified pulses reaches up to 4.3 W. The third stage is to compress the time width of amplified pulses in compressor unit. Upon completion of these stages, the output laser pulses have a time width around 60 fs, the value of the average power approximately 3.5 W, and the spectra of these pulses has a pick at 800 nm. At this point the laser system generates ultrafast near-infrared laser with pulse duration around 60 fs. Figure 3.7 shows the process of developing the pulse amplitude of the laser inside the Regen.

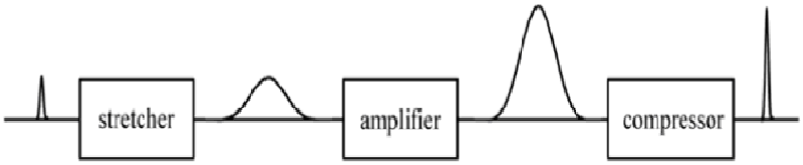

Figure 3.7: Diagram showing the pulse amplitude stages.

Our work will utilize these pulses as a pump to excite the topological insulator sample. The visible laser pulses generated by the amplifier are divided into two parts by a beam splitter. One part is directed to use as a pump with 800 nm, and the other part goes to OPERA to generate 4 μm probe.

3.4.4 Optical Parametric Amplifier

An optical parametric amplifier (OPA) acts as a passive laser device that transforms a monochromatic signal into output a tunable wavelength laser. There are several non-linear crystals that are utilized in OPA to modify the wavelength through Parametric Amplification, Super-Continuum Generation and the processes of Difference Frequency Generation [81]. The OPA consists of three stages in order to generate variable wavelength output. An initial stage of the process consists of splitting the monochromatic input into two beams. Approximately %10 of it is directed towards a Sapphire plate for the generation of continuous white light (seed beam). The remainder of the beam is directed directly into the second and third stages of amplification (pump beam). The production of white light results from self-phase modulation occurring within the crystal. As the pulse passes through the Sapphire plate, there is a nonlinear optical Kerr effect, resulting in changes in the refractive index of the material as a function of the pulse

intensity profile. Consequently, this variation creates a phase change dϕ in time that corresponds to the modification of the spectrum ($\Delta\omega = \frac{d\phi}{dt}$).

Following the sapphire plate, a dispersive plate is employed in order to extend the pulse over a wide range of frequencies in time. A second nonlinear stage occurs with the pump amplifying the seed beam using OPA process as illustrated in figure 2.9. The arrival time difference between the seed beam and the pump beam on the nonlinear crystal is adjusted to select a specific wavelength at this stage of the process. Nonlinear crystal angle (Beta barium borate, BBO) is selected to ensure the phase-matching condition of the signal pulses and pump. Additionally, a third amplification stage utilizes the OPA, which further amplifies the signal beam via, along with another beam (Idler)$\omega_{Idler} = \omega_{pump} - \omega_{signal}$ that emerges. Changing the frequency of the signal beam can adjust the frequency of the idler beam. Nevertheless, the real case could be more complicated. Because the pump beam has a high intensity, additional nonlinear processes, for instance, fourth harmonic generation, could develop in nonlinear crystals, leading to multi-wavelength output. Thus, dichroic mirrors are used for separating beams of different wavelengths and directing them in different optical directions in accordance with experimental needs. A diagram of the process inside the OPA and the levels of energy is shown in figure 3.8.

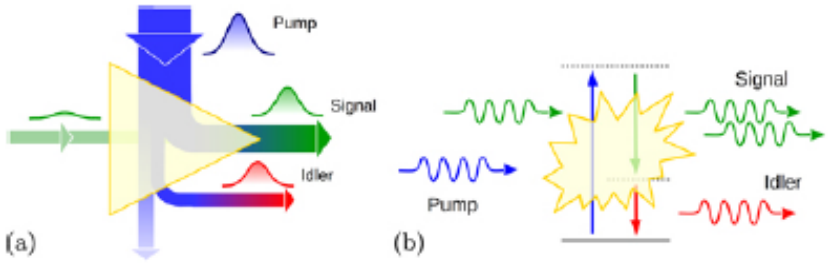

Figure 3.8: The OPA process illustration (a) and the diagram of the energy levels (b) [82].

In our study, we used a probe with a 4 μm, which was selected from the output of an optical parametric amplifier.

3.5 Pump Probe Technique

Several physical phenomena occur at extremely fast rates in the natural world, such as atomic movement, vibrations of molecules, photon absorption and emission, and scattering processes. Processes such as these may take place on timescales as short as a few picoseconds ($10^{-12}s$) or femtoseconds ($10^{-15}s$). A detailed view of these fast processes is crucial to gaining a better understanding of the mechanism of matter's excitations, providing a basis for great improvements in the precision of time-resolved measurements over the last few decades. For accurate measurement of ultrafast processes, timing uncertainties should be less than the process timescale, necessitating temporal resolution on the order of $10^{-15}s$. A pump-probe spectrometer is one of the most common methods for studying time-dependent phenomena, and it has led to advances across a wide range of fields. Pump probe measurements are performed by splitting the laser pulse from a laser pulse generator into two separate laser pulses: a stronger 'pump' pulse and a weaker 'probe' pulse as shown in Figure 3.9.

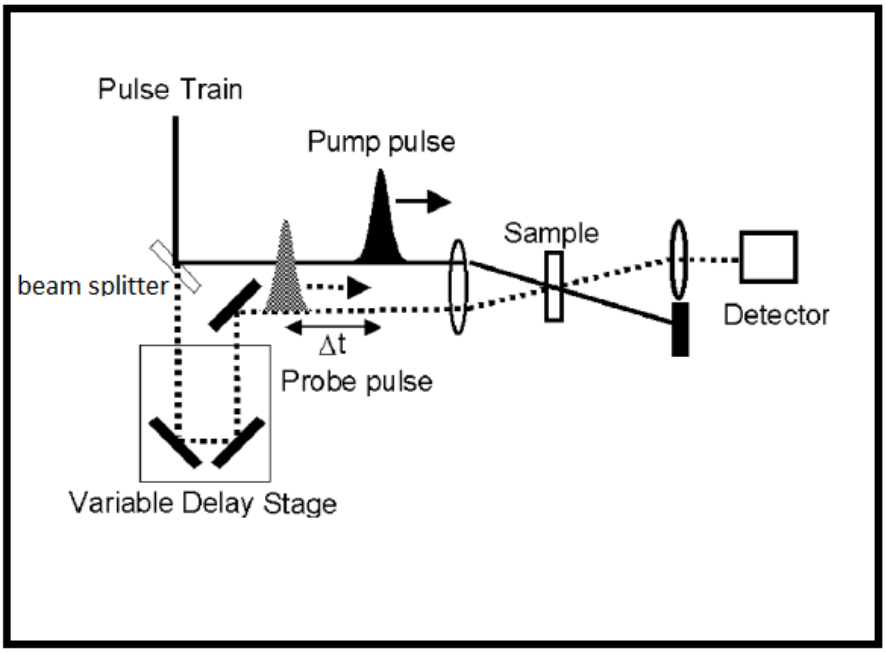

Figure 3.9: The pump probe set-up, where the laser pulse is separated into pump pulses and probe pulses by beam splitters. To control the delay time between the pump and probe, the probe pulse is directed to the delay stage. Before the probe reached the detector, the pump and probe overlapped on the sample.

In order to study dynamical processes employing pump-probe spectroscopy, the physical system has to be perturbed from its equilibrium state. This is achieved with the pump pulse, which has to travel a shorter distance than the probe, so that it can arrive at the sample first. The sample is excited by the pump pulse, and can be altered in many different ways, such as intensity, energy, polarization and duration. This makes it possible to manipulate the sample in whatever way is needed. For an illustration of this process, consider electron energy levels in an atom. When the energy of the pump pulse equals the difference between the two levels, photons of the pump pulse are absorbed by atoms in the sample. This leads to an increased concentration of electrons at the higher energy level. Afterwards, the probe pulse reaches the sample, which is often time delayed after the pump pulse has perturbed it. By varying the path length difference between pump and probe pulse, the delay time between the pump and probe pulse can be controlled.

The probe pulse interacts with the sample but does not change it states, which is then measured by the detector. This allows the determination of the physical state of the sample, since it eventually decays to an equilibrium state after the perturbation caused by the pump pulse. The pump-probe technique can either measure reflection probe or transition probe, depending on the case being studied. Our purpose in this study is to measure the reflection spectrum and analyze the results to conclude about the electronic surface of the TI sample. This work was conducted in order to investigate the ultrafast dynamics processes of the excited carriers on the surface of the sample. To provide a better understanding of the processes that occur during the pumping process, the following section will describe the typical processes occurring following the excitation. We will use the reflection signal of the probe and its polarization state to determine these processes.

3.6 Excitation and Relaxation

Electrons become excited when they are promoted from their ground state to a more energetic one. This is can be accomplished through photoexcitation (PE), which involves an electron absorbing a photon and gaining its energy. In semiconductor crystal lattices, thermal excitation occurs when vibrations in the lattice move electrons to a higher energy state.

The interaction between ultrafast laser pulses such as picosecond or femtosecond lasers and semiconductors , enable an opportunity to study fundamental physical processes occurring in condensed matter. A femtosecond laser pulse and the pump-probe method, however, provide a more detailed demonstration of the process, which indicates by which the energy in the laser pulse is delivered first to the electrons and then to the lattice. The different mechanisms of carrier excitation and relaxation are distinguished by their distinct characteristics. First, there is carrier excitation, which is followed by redistribution, thermalization, and free carriers cooling via scattering, which is followed by carrier-lattice thermalization, which is followed by the free carriers recombination and diffusion , result-

ing in a decrease in carrier density, and lastly thermal structural effects. These processes occur in no particular order, rather they may occur in the same or overlapping period of time. For instance, in some materials, carriers can distribute their thermal energy amongst one another while at the same time they cool by passing energy to lattice phonons. However, in semiconductors, the excitation and relaxation processes usually take place at timescales between picoseconds and femtoseconds during pumping operation.

3.7 Excitation Mechanism

As a result of the interaction between visible light and a solid, the first process is excitation, which occurs at the surface of the solid. According to the different mechanisms used to excite the carriers in semiconductors, the electrons can be excited in a variety of different ways. SPA (single photon absorption) is one of the most common mechanisms for excitating electrons when the phonon energy exceeds the band gap, and it is the most common method of excitating electrons [83]. Accordingly, this process is known as interband absorption, which generates an electron-hole pair and increases both the energy E and the number density of excited electrons N. In Figure 3.10, it can be seen that there are direct and indirect band gaps in the absorption process of single phonons.

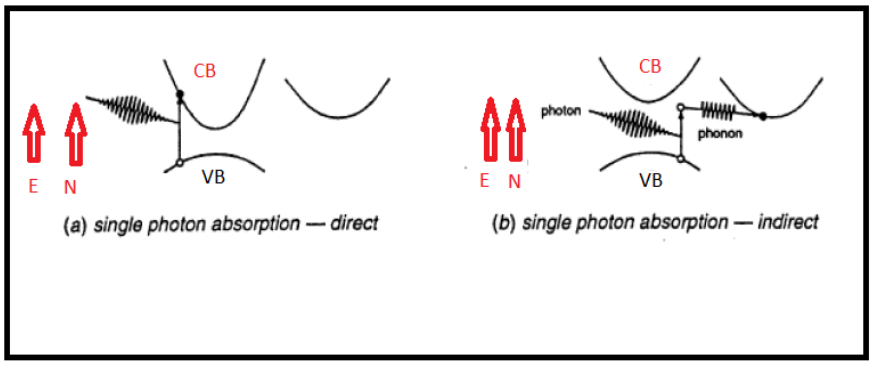

Figure 3.10: The two types of absorption processes,(a) direct band gap and (b) indirect band gap.

In semiconductors with an indirect band gap. A single photon can still be absorbed

with an energy higher than the band gap, but this process should conserve momentum through phonons.

The energy of the photons may be lower than the energy gap in some cases, meaning that multiphoton absorption (MPA) will be a significant factor in the case in which the photon energy is lower than the energy gap. The probability of MPA occurring is much lower than that of SPA. In spite of this, there is, in fact, an increase in the rate of (MPA) with increased intensity, which is the reason why it becomes more significant in extremely intense pulses of light [84]. Figure 3.11 illustrates the MPA where the phonon energy is lower than the band gap.

On the other hand, the excitation could be caused by free carriers that are well excite to the conduction band and increase the number of free carriers by impact ionization [85]. It is possible for one or more of these excitation processes to occur when laser pulses interact with semiconductors, depending on many different factors.

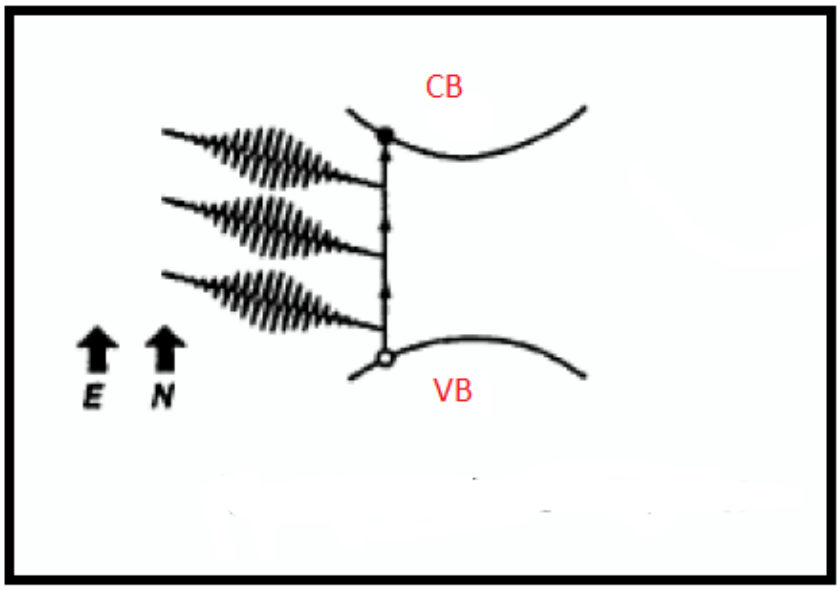

Figure 3.11: An absorption of multiple photons with a photon energy below the band gap, resulting in increased energy and carriers density.

3.8 Free Carriers Relaxation

The free electrons and holes produced by a relatively monochromatic laser pulse will be excited to a specific point in the band structure where the energy difference between the excited and ground states $E_v - E_c$ will be equal to the incident photon energy. Figure 3.12 illustrates the photoexcited process where carriers are deposited at particular points in the band based on the energy of the incident photon. After excitation, the holes and electrons are redistributed within the conduction and valence bands through carrier-phonon scattering and carriers-carrier scattering. Figure 3.13 shows the excited carriers re-distribution in both the conduction and valance bands following the excitation process where the dark shadow region represents the carriers density. The excited carriers populations rapidly reach the Fermi-Dirac distribution. It is important to note that the number of carriers has not changed at this point. It is due to the emission of phonons during the scattering process that energy is transferred from the carriers to the lattice, resulting in a decrease in carrier energy E.

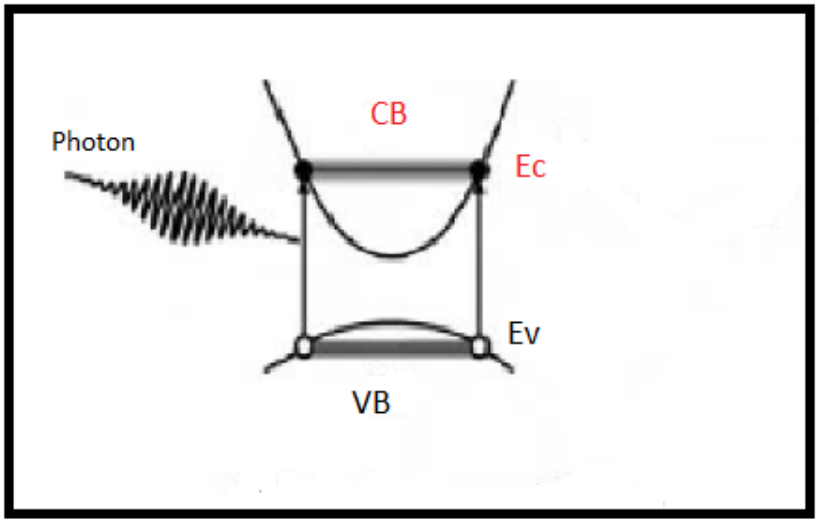

Figure 3.12: Excites carriers in specific states in the band according to the energy of the excited photons [86].

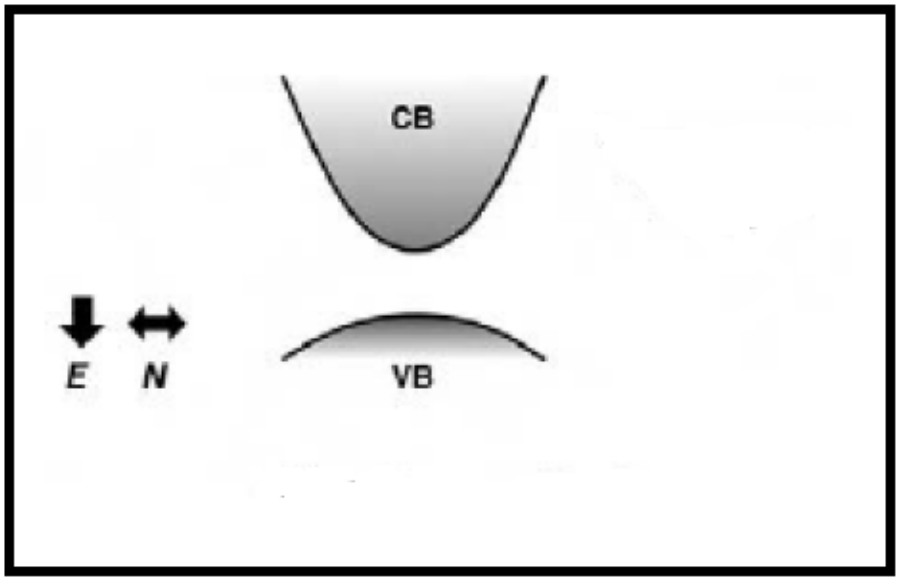

Figure 3.13: The redistribution of the carriers after scattering within the conduction and valence band [86].

Carrier-carrier scattering is the result of two carriers colliding that occurs as the result of collisions. Figure 3.14 shows that carrier-carrier scattering occurs within the conduction band where the total energy remains unchanged. The interactions between carriers are determined by the Coulomb effect between the free carriers. This scattering has no effect on the total energy or the rate of carriers, but the energy and momentum of individual carriers are determined by multiple scattering events. Considering that scattering involves two bodies, the probability of scattering must increase with density. It has been shown in experiments that scattering times vary depending on which estimates are used. For instance, Oudar et al. employed transient transmission spectra to obtain $0.3 \mp 0.1ps$ as an excitation time when the carriers density was 10^{18} [87]. Meanwhile, Elsaesser et al. obtained the time of the carrier-carrier scattering in the range of 100 femtoseconds or less in the case where the density of the excited carrier is estimated to be $1.7 - 7.0 \times 10^{17}$ by using time-resolved measurements [88]. The scattering rate is predicted to be dependent on $N^{-1/3}$ in Monte Carlo simulations [89] However, when the carrier density reaches a certain level($10^{20}cm^{-3}$), screening tends to decrease the strength of the Coulomb

interaction between carriers, therefore reducing the cross section of scattering that occurs as a result. There is not a constant increase in the scattering rate as density increases, and it is also possible that it could decrease at higher densities as well.

On the other hand, energy and momentum can be lost (or gained) via emitting or absorbing phonons or by vibration of the lattice. In semiconductors, carrier-phonon scattering can be divided into two general categories. When the carriers scatter in the same valence or conduction band, it is called intravalley scattering. However, when the carriers scatter in a different band, it is inervalley scattering [90]. Figure 3.15 illustrated intravalley and intervalley scattering where the total energy decreases while the number of carriers remains unchanged. It is important to note that, in general, whether inervalley or iravally scattering is occurring, it will always be a two-body process.

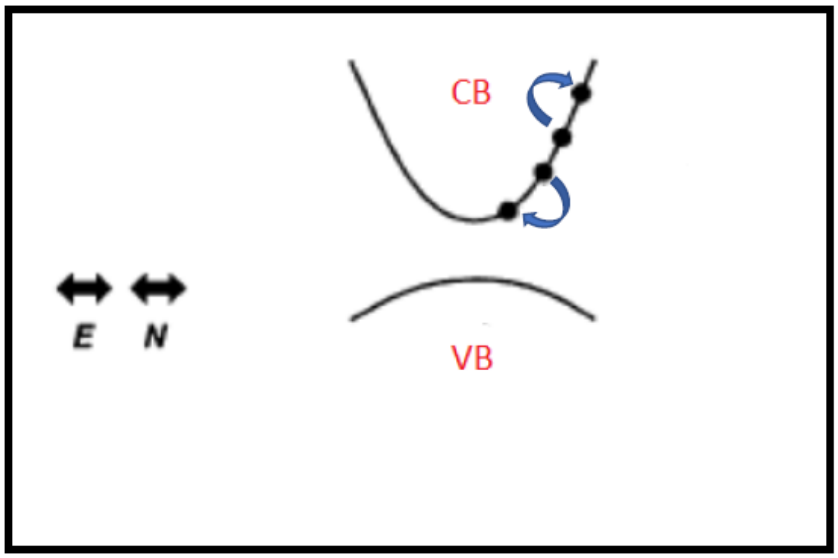

Figure 3.14: Carrier-carrier scattering within the conduction band where the energy and density of carriers remain unchanged.

The rate of scattering or collision number per second, approximately linearly depends on the carriers number N and on phonons number. However, in the presence of high carrier densities, this linear relationship no longer applies due to screening effects. A

carrier-lattice thermalization occurs when carriers transfer their energy via optical or acoustic phonons to the lattice. Studies have shown that optical phonons are generated primarily by intravalley scattering, whereas acoustic phonons are produced by intervalley scattering [91, 92, 93]. The lattice and free carriers will be at the same temperature at this point.

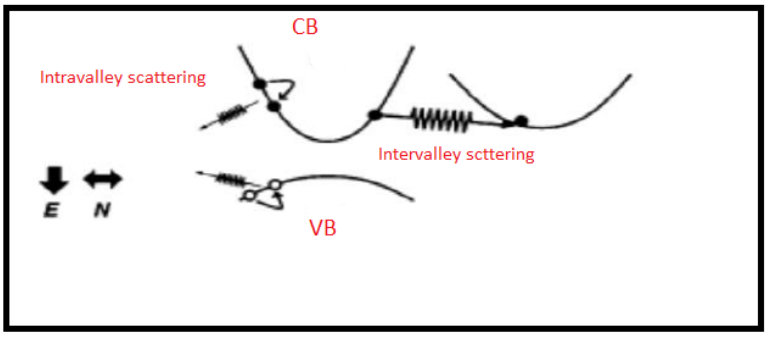

Figure 3.15: Carrier-phonon scattering where the energy is reduced while the density of carriers remains unchanged.

3.9 Carriers Recombination

Following the scattering process, even though the carriers after redistribution and the lattice have the same temperature, there is also an excess of free carriers in comparison with the actual thermodynamic equilibrium. The carriers can be removed via two mechanisms: electrons and holes recombination or carriers diffusion. Recombination and diffusion may occur before carrier-lattice thermalization. There's a possibility that carriers recomination could occur faster than carrier lattice thermalization.

The excess energy can be removed from electrons and holes when they recombine by different processes. Firstly, radiative recombination which emits a photon. Secondly Auger recombination, when the release energy can be taken by another electron or hole. The third mechanism is recombination by surface states and defects. Figure 3.16 shows

these recombination processes.

Each of the three processes reduces the free carriers number. Auger recombination has no effect on the total energy of the carriers; in contrast, carrier average energy rises as density decreases. One, two, or three carriers are involved in defects, radiative recombination, and Auger recombination, respectively.

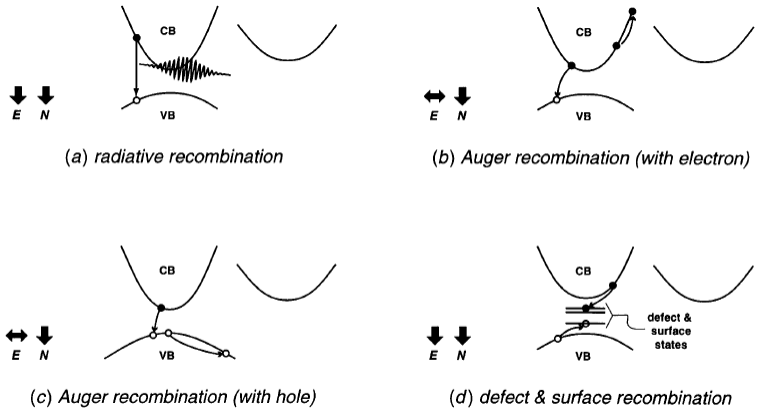

Figure 3.16: A different mechanism of recombination in which the number of carriers decreases in all processes. However, the energy remains the same in Auger recombination while it decreases in radiative and surface recombination [86].

Consequently, their rates are determined by density N, N^2, and N^3, respectively, and the equation for the combined recombination rate can be written as follows [94]:

$$\frac{dN}{dt} = -AN - BN^2 - CN^3 \tag{3.1}$$

Where A, B, and C represent defect recombination, radiation recombination and Auger recombination respectively. It is significant to note that, when the density exceeds $10^{20} cm^{-3}$, there is a predicted decrease in the coefficients of recombination in proportion to N as a result of the screening effects of the mobile carriers. Screening decreases the Coulomb interaction between free carriers, or between free carriers and defects, thereby decreasing the likelihood of recombination [95]. As a consequence, for high carrier densities, the rates of all three recombination do not remain to increase with density at the same rate

as expected in Eq 3.1. In comparison with carrier recombination, the number of carriers remained unchanged with diffusion. On the other hand, diffusion removes the free carriers away from the excited region. Figure 3.17 provides corresponding times for the different processes, meant to reflect the probability of occurrence of certain times when the excitation strength changes.

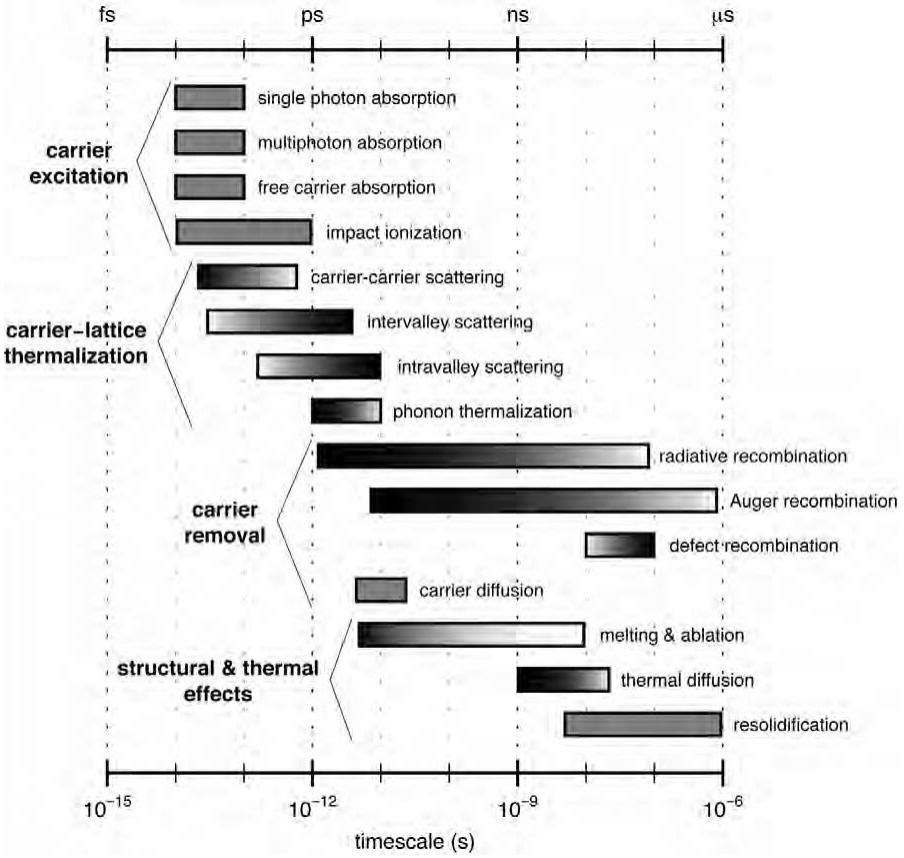

Figure 3.17: the figure shows timing characteristics for a variety of electron and lattice dynamical processes in semiconductors, such as carrierlattice thermalization, carrier removal, and structural and thermal changes. The bars represent a broad range of characteristics over time. A gradient in the bar indicates the presence of a known dependence between a characteristic time and carrier density in a process. High densities represent the dark end while low densities indicate the light end. There are some cases where carrier density is not dependent on the process (e.g., excitation) or when the dependence is not well understood (e.g., diffusion). In these cases, the bars are gray [86].

CHAPTER 4

RESULTS AND DISCUSSION

4.1 Time Resolved Visible Pump-IR Probe Measurements

The main motivation for this work is to study the dynamics of excited charge carriers on the surface of TI sample using IR probe. This method allows to probe optical processes on the surface that occur in IR spectrum region following excitation the surface by optical pump with a femtosecond pulse that has energy above the band-gap of the sample. Visible pump have been used previously to investigate optical processes in TI [96], but IR probe have been used relatively rarely. A coherent ultrafast laser system is used in the setup as described in Chapter 3. The laser output from 'Regen' was split into two beams using a beam splitter. The smaller portion of the beam which is approximately %5 was employed as the pump beam for excitation the free charge carriers. The remaining portion of the beam was directed into an optical parametric amplifier (OPA) to produce a probe beam as it shown in Figure 4.1. The visible pump incident angle was set to 30^0, while the incident angle of the IR probe was set to 79^0 which is the Brewster angle of the sample at 4 μm. The purpose of using Brewster angle is to study the polarization dependence which makes the measurements highly sensitive at this angle. For this experiment, in order to achieve a desired delay between the pump and probe signals, a reflector mounted on a motorized translation stage was used.

It is possible to obtain the precise distance at the delay stage. This can be achieved from the relation

$$c = x/t \tag{4.1}$$

, where c represents the light velocity,x is the distance, t is the delay time between pump and probe . A LabView program was used to adjust the delay time between the pump and the probe.

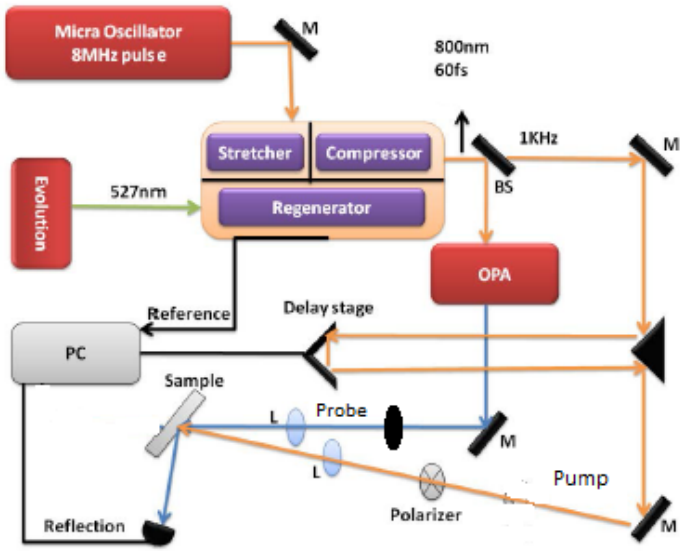

Figure 4.1: Schematic illustration the setup of the pump-probe. the laser beam from the amplifier is split into two parts to represent the probe and the pump . The delay stage has been used to achieved the requested length of optical path between probe and pump. A LabView program is used to control all the parts of the setup.

The measurements of pump-probe experimental results have been presented as a change in the reflectance signal, $\frac{\Delta R}{R_0}(\Delta t) = \frac{R_e(\Delta t) - R_0}{R_0}$. Where R_0 represent the reflectance from the unexcited sample. while R_e Reflectance from the sample after excitation as a function of the probe delay, Δt.

The measurements were conducted with different pump polarization stations at Brewster angle using 250 mW pump power in room temperature. The Brewster angle was calculated by measuring the reflection signal with a p-polarized probe with different inci-

dent angles. When the reflection signal dropped to a minimum value. It is at this point that the incedent angle with the lowest reflection signal represents the Brewster angle for the wavelength of the probe. Based on different pump polarizations, Figure 4.2 shows the change in $\frac{\Delta R}{R_0}$ signal with different polarization states of the pump as a function of delay time with p-polarized pump . It was measured that the probe had the highest value of $\frac{\Delta R}{R_0}$ at a p-polarized of the pump (red curve). While at 45^0 pump polarization, the peak of $\frac{\Delta R}{R_0}$ (green curve) was half as much as the peak when the pump was p-polarized. However, the change in reflectance signal remains unchanged with the S-polarized pump (blue signal).

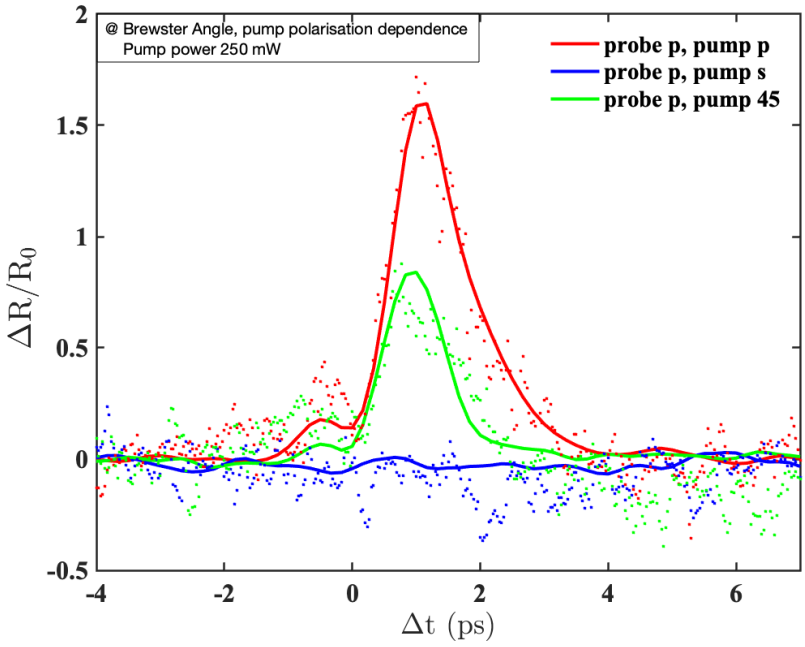

Figure 4.2: Change in differential reflection of the probe signal with three pump polarization states.

A second set of pump probe measurements has been performed using various pump powers. Both the pump and probe are p-polarized. As can be seen from Figure 4.3, the maximum of $\frac{\Delta R}{R_0}$ signal increases with pump power. Refractance peaks are illustrated in Figure 4.4 based on different pump powers.

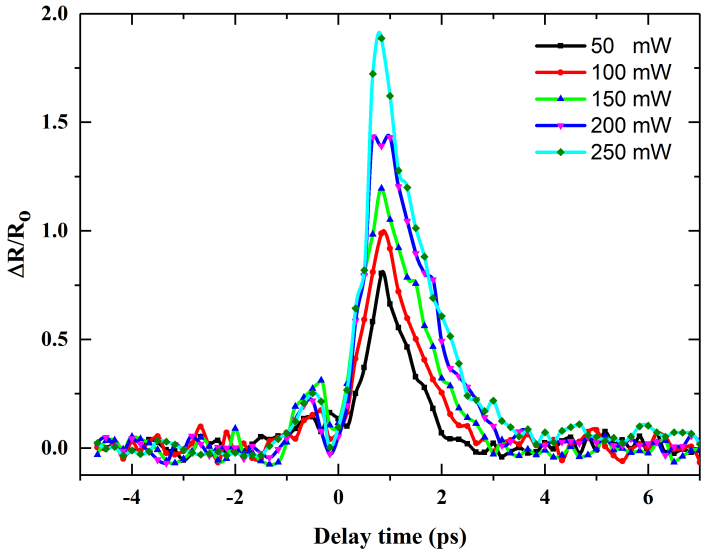

Figure 4.3: Change in reflectance signal at Brewster angle with different pump power.

Increasing pump power increases the peak of $\frac{\Delta R}{R_0}$ signal as more excited carriers are generated. Figures 4.5 and 4.6 show the decay time fitting with error bars at different pump powers as a function of the delay time between pump and probe. The results indicate that the decay of the reflectance change signal increases with pump fluence, as shown in Figure 4.7. Moreover, there was no apparent change in the rising time with different pump powers, which was 0.3 ps with different pump powers.

Rise and decay times were estimated by fitting normalized single exponential curves of form $y = b\exp(-x_0 + x)/\tau_r$ and $y = a\exp(x_0 - x)/\tau_d$ respectively, with arbitrary coefficients $a = b = 1$ and the rise and decay times τ_r and τ_d respectively used as fitting parameters. The time x_0 has no physical meaning as zero time - it just shifts the exponential curve to the fitting points.

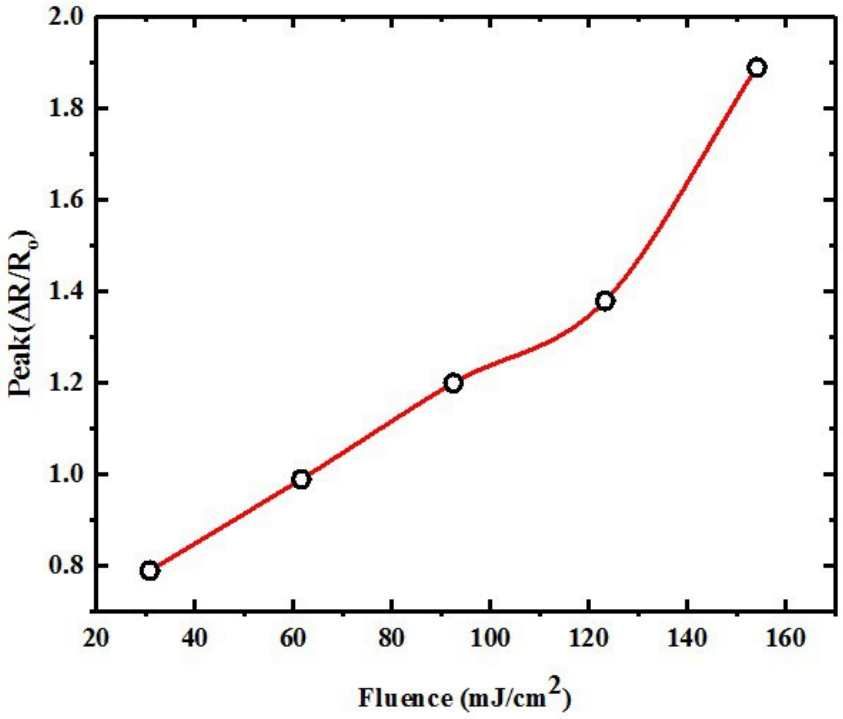

Figure 4.4: The maximum reflectance peak with different pump power.

Figure 4.8 illustrates the increasing number of carriers N when the fluence of the pump increases. Where the carriers density $N = \frac{(1-R)(F*\alpha)}{\hbar * w}$, R is the reflectance, F is the fluence, α is the absorption coefficient measured from ellipsometry, $\hbar$ is Planck constant and w is angular frequency of the pump. The fluence $F = \frac{P}{Hz*A}$, where P is the power, HZ repetition rate of the pump(1 kHz), A is the beam area, where the pump diameter 620 μm.

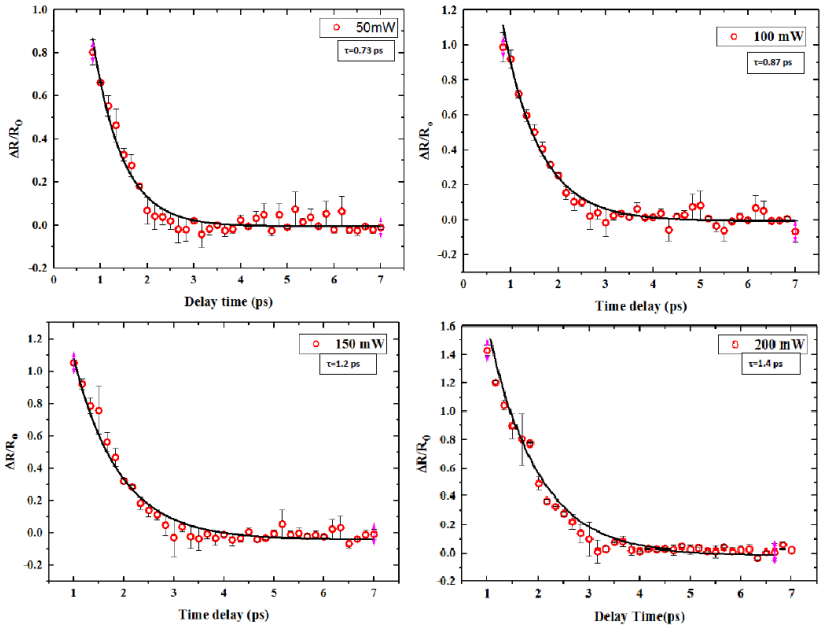

Figure 4.5: Graph showing decay time fitting with error bars for different pump powers (50,100, 150, 200 mW) and different probe-to-pump delay times.

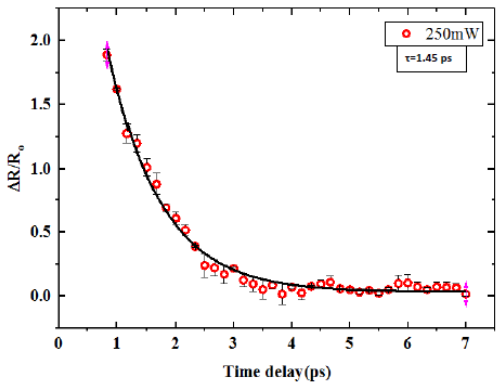

Figure 4.6: With varying probe-to-pump delay times, a decay time fit is shown with error bars at a pump power of 250 mW.

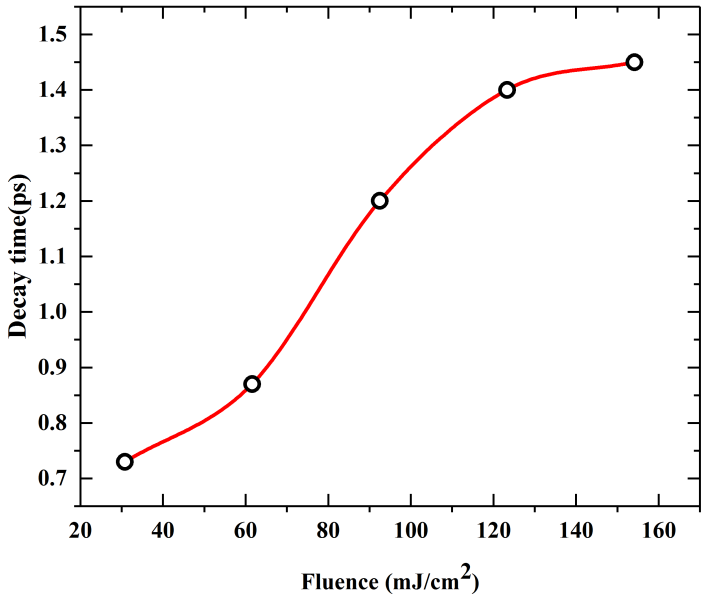

Figure 4.7: The decay time of different signal as a function of pump fluence .

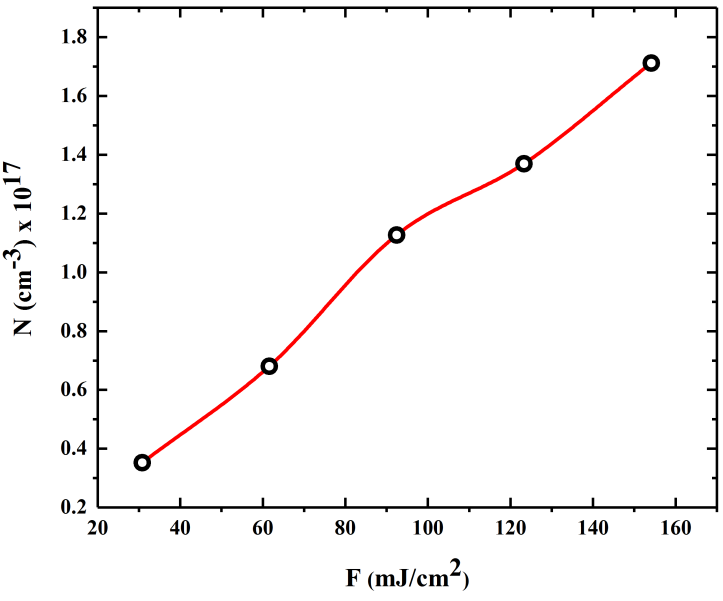

Figure 4.8: Density number of carriers with various laser pump fluences..

4.2 Discussion

For pump probe techniques, the probe energy plays an essential role in exploring the dynamic carriers of the sample surface. The work in this thesis uses an IR probe (4 μm), which is very uncommon in the literature. The majority of studies using the pump probe technique employed probe energy much higher than the band gap of (TI) [10, 97, 98, 96, 99, 15, 12, 13], Based on previous studies with visible probe, the typical reflectnce signal as a function of probe delay consists of three oscillations. These oscillations induced by electron-electron interactions, optical phonons and acoustic phonons. Additionally, there is also a long decay time that is related to hot carrier recombination (approximately 1 ns) [15, 96, 10]. When using a visible probe, the electronic state that is being monitored may differ from that monitored by an IR probe. In other words, IR probes interact with different states in the sample than visible probes interact with. Furthermore, since the visible probe energy is higher than the band-gap of the sample, the probe photons can excite more carriers via interband transitions. IR probes do not produce interband excitation, indicating only free carriers in the conduction band.

By comparing the results we obtained with an IR probe, we found that there is only one peak differential reflection signal with ultrafast decay. Firstly, if we assume that free carriers on the surface interacted with the probe photons, we should observe a negative signal as a result of IR absorption by free carriers. Following the excitation, there is a positive signal that indicates an increase in reflectance.

The positive signal can be induced by the surface plasma wave that is generated by the pump photons on the surface of the sample. The differential signal observed with a p-polarized pump and absent with a s-polarized pump supports the idea that surface waves produce the signals. The Figure 4.9 illustrates the change in reflectance signal with p-polarized and s-polarized pump. The result indicates that the signal with s-polarized pump remains unchanged.

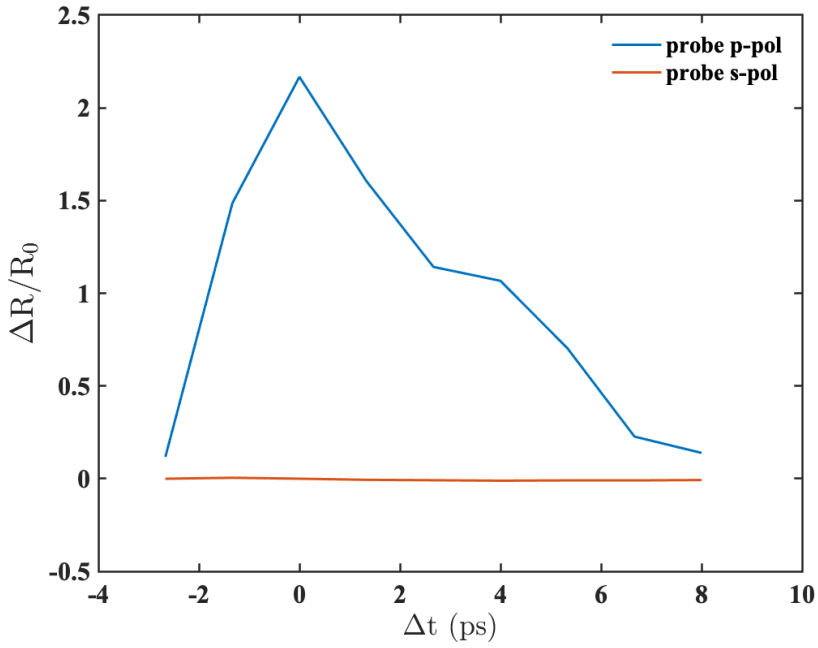

Figure 4.9: The change in reflectance signal with p- and s-polarized pump.

A positive signal may be explained by an increase in reflectance caused by screening of the probe electric field by the plasma wave. If we assume that a surface plasma wave is generated on the sample surface following excitation. Screening and total reflection occur with the incident probe when the probe frequency is lower than the plasma frequency. With an IR probe with a frequency below surface plasma, it is possible to observe plasma waves on the sample's surface. This is one of the reasons for using infrared probes, because the plasma frequency in semiconductors is in the IR region. [100].

Our measurements show that the decay time of the surface plasma increases with pump power. In order to explain the prolonged lifetime of plasma waves with the pump fluence, it is necessary to realize that the surface wave is generated on the surface as a result of the coherent oscillation of free carriers. Therefore, increasing the lifetime of free carriers oscillation leads to an increase in plasma wave lifetime. According to our measurements, the recovery time of free carriers increased with pump fluence, which is in agreement with previous studies [101]. The prolonged decay time was due to the recovery time of electrons in the Dirac cone becoming less effective with higher pump fluence [102]. When the pump

fluence increases, the Dirac point reaches the Fermi level. Due to this, the phase space in the Dirac cone becomes smaller, and as a result, the scattering process decreases. When scattering decreases, the lifetime of free carriers increases, thereby increasing the decay time of the plasma wave.

According to another study, the decay time increases with the pump fluence, based on a two-temperature model [103, 104]. Typically, this model is used to describe free carriers dynamics in metals. Due to the fact that TI contains metallic surface states, this model could be applied to estimate the free carriers in our sample. According to the two-temperature model, the sample is considered as a synthesis of two components, the lattice and electron. The two-temperature model demonstrates that as pump fluence increases, electron temperature increases, resulting in a longer decay time.

Our time-resolved measurements provide valuable insight into the generation of plasma waves on the surface of TI. It is possible to use the fast decay of the plasma wave as an ultrafast optical switch in optical devices and optical communication systems.

CHAPTER 5

TIME-RESOLVED ELLIPSOMETRY MEASUREMENTS

5.1 Introduction

This chapter presents the Ellipsometry technique that we have employed to study the dynamics of the free charge carriers on the surface of the sample. In order to achieve this goal, we determined the surface's complex refractive index following the excitation. Utilizing a visible pump and an infrared probe, we developed a time-resolved ellipsometry set-up.

5.2 Reflectance Of The Light

In typical measurements, the reflectance R is calculated as the ratio of I_r/I_i where I_r is the reflected light intensity, and I_i is the incident light intensity. The reflectance of p- and s-polarized light is then given by

$$R_p \equiv \frac{I_{rp}}{I_{ip}} = |\frac{E_{rp}}{E_{ip}}|^2 = |r_p|^2 \tag{5.1}$$

$$R_s \equiv \frac{I_{rs}}{I_{ip}} = |\frac{E_{rs}}{E_{is}}|^2 = |r_s|^2 \tag{5.2}$$

Where E_P and E_S the electric field in p- and s-polarized respectively. In general, wave-

length, polarization, and incident angle determine the reflected and transmitted light. If we want to understand how light reflects, then we should consider light as an electromagnetic field.

When light waves interact with a material, small oscillations in polarization occur in the atoms or electrons in the case of metals. This lead to emit a radiation waves from each oscillation particle in all directions, same as a dipole antenna. All of these waves combine to create specular reflection and refraction. Figure 5.1 illustrates how a dipole responds to an electric field that generates light.

In dielectric materials, the electric field of incident light interacts with the electrons within the material, resulting in electron movement and producing new radiators. In glass, for example, the reflected light is the sum of all the backward radiation of the electrons. While a combination of the forward radiation wave generates the refracted light.

Radiation process illustrated in Figure 5.1 where the dipole oscillates by applying an electric field. In order to understand the process, we can consider the dielectric medium as a parallel plate capacitor and the incident light as an electric field. When an electric field is applied to a medium, the positive and negative charges within it experience opposite electric forces. Once the dipoles are formed, they oscillate as the electric field changes to create radiation.

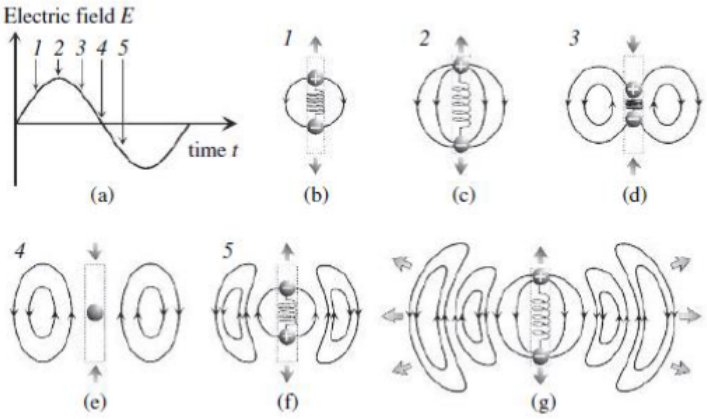

Figure 5.1: Radiation from electric dipoles in a dielectric: (a) an alternating electric field applied to the dielectric, and $(b) - (f)$ show the response of the electric dipole to an external electric field of $1 - 5$. [100]

In metals the free electrons without any binding energy oscillate with incident light to generate the reflected light

5.3 Brewster Angle

In our work, all the measurements have been taken at Brwester angle. At Brewster angle r_p and r_s have the maximum difference, which leads to be the sensitive angle for the measurements. For this reason, ellipsometry measurement is typically conducted at the Brewster angle. In general at Brewster angle, the reflectance value of r_p reaches zero, as a result the reflectance will be only r_s. The polarization angle or Brewster angle phenomenon can be explained by radiation of an electric dipole at the interface. In this situation, the radiation of an electric dipole emerges from the atoms that reside close to the interface, and only light waves that obey the law of reflection($\theta_i = \theta_r$) are reflected back as shown in Figure 5.2.

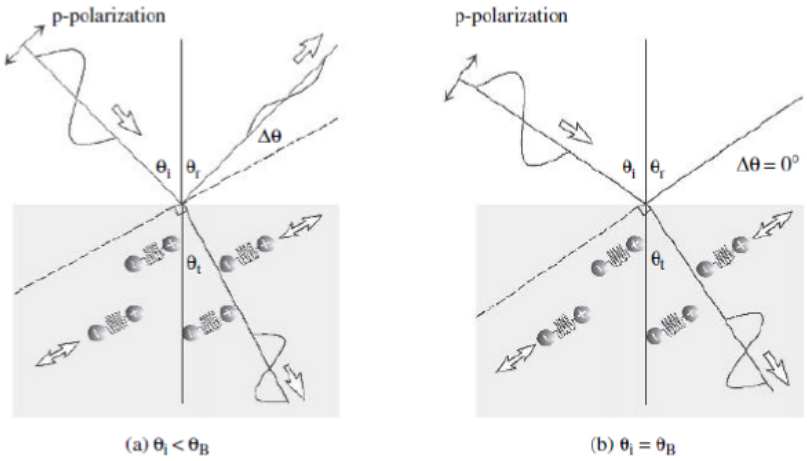

Figure 5.2: Radiation of dipole at (a) $\theta_i < \theta_B$ and (b) $\theta_i = \theta_B$ [100].

The figure 4.2 shows $\Delta\theta \neq 0^0$ the angle between the direction of oscillator dipoles and the direction of reflected when $\theta_i \neq \theta_B$. However, figure 4.2 shows when $\theta_i = \theta_B$, then $\Delta\theta$ becomes zero, as we illustrated in figure 4.1 there are no emitted waves toward the direction of oscillator dipoles. In other words, the reflected light becomes nonexistent at the angle when the direction of oscillator dipoles is perpendicular to the direction of vibration reflected light. Due to this, $R_p = 0$ at θ_B. In contrast, the direction of dipole oscillations is always parallel to the vibration of reflected S-polarization. This causes R_p to slowly increase with increase θ_i. Consequently, at Brewster angle s-polarized and p-polarized light exhibit significantly different reflectance profiles.

5.4 Ellipsometry Principal

Ellipsometry is an optical measuring technique that determines the polarization state of light reflected from surface. One of the main features of ellipsometry is that it measures the difference in polarized light generated after a sample reflects light. According to ellipsometry measurement, the polarized states of reflected and incident waves are determined according to their polarization coordinates, s- and p-polarizations. An ellipsometry technique measures the difference between amplitudes and phase differences between s-

polarized and p-polarized light. In general, spectroscopic ellipsometry measurements have been conducted in the visible/ultraviolet spectrum, however, the measurements have also been conducted in the infrared spectrum. The method of spectroscopic ellipsometry is generally used for measuring the thickness of thin films and for measuring optical constants for the samples. In contrast to reflectance/transmittance measuring, ellipsometry provides the precise measurement of a refractive index n and coefficient of extinction k, these are known as the optical constants. Figure 5.3 shows the principle of ellipsometry measurement set-up, where light that is incident has linear polarization and is directed at $+45^0$ with respect to the E_{ip} axis. Particularly, $E_{ip} = E_{is}$ can be demonstrated with this polarization, as the amplitudes of s- and p-polarizations equal each other and the difference in phase between them is zero. According to our discussion earlier in reflectance of the light section (5.3), reflection amplitudes for s- and p-polarizations are different considerably as a result of a difference in the radiation of electric dipoles. Therefore, when light is reflected from a sample, s- and p-polarizations exhibit different phases and amplitudes. In ellipsometry, as a result, the difference in reflection of light with s- and p-polarizations is determined as the change of polarization state. Particularly, for simple sample structures, an amplitude ratio ψ is described by a refractive index n, and Δ corresponds to light absorption expressed as an extinction coefficient k. As a result, two of the parameters (n, k) can be obtained easily by using the two ellipsometry parameters (ψ, Δ) determined from Fresnel equation measurements. Ellipsometry measurement is based on this principle. The (ψ, Δ) values measured by ellipsometry can be calculated according to the reflecting amplitude coefficient ratios for s- and p-polarizations [100]:

$$\rho \equiv \tan\psi \exp(i\Delta) \equiv \frac{r_p}{r_s} \tag{5.3}$$

When measuring light transmission, rather than light reflection, (psi, Delta) is defined as follows:

$$\rho \equiv \tan\psi \exp(i\Delta) \equiv \frac{t_p}{t_s} \tag{5.4}$$

The optical constants (n.k) can be obtained from the ellipsometry angles ψ and Δ via the Stocks parameters (which will be discussed in the subsequent section). From (n,k), other parameters, such as the absorption coefficient and complex dielectric constant, can be determined. In ellipsometry, the angle of incidence is selected accordingly that the accuracy for the measurement is optimized. For semiconductor measurement, the incidence angle usually ranges from $70^0 \rightarrow 80^0$.

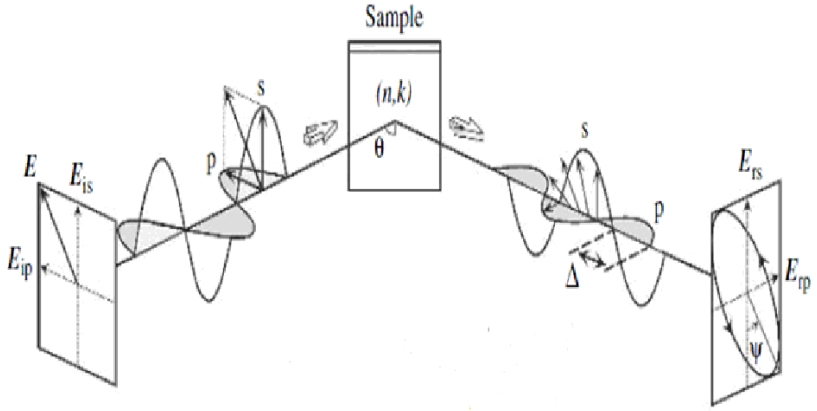

Figure 5.3: The ellipsometry set-up.

As previously mentioned (in the reflection of light section), the coefficient of amplitude reflection for s- and p-polarizations changes considerably depending on the variance in radiation of the electric dipole. Therefore, upon reflection of light on a sample, s- and p-polarizations exhibit different amplitudes and phases. ellipsometry measurements calculate the two values (psi, delta) that represent the ratio of the amplitude and the difference in phase between p- and s-polarizations, respectively. In the spectroscopic ellipsometry, in consequence, the difference of the reflection of light with p- and s-polarizations is calculated as the difference in state of polarization. Particularly, the ratio of amplitude (ψ) is represents the refractive index n, while Δ characterized by absorption of light determined by the extinction coefficient k. In this instance, (ψ) and Δ the two ellipsometry angles can directly calculate n and k. In other words, this is the core principle of measurement with ellipsometry. The various ellipsometry methods and Stokes parameters will be explained

in this chapter, followed by results and discussions.

5.5 Poincar Sphere

A point on a sphere can represent the state of polarization if we consider Stokes' parameters (S_{1-3}) as the axes of the three-dimensional coordinate system. Figure 5.4 illustrates this sphere, which is called the Poincar Sphere. Poincar's Sphere itself displays the total intensity of light S_0. If Poincar's Sphere is compared with the earth, then the polarization on the equator is linear. Linear polarization differs with respect to an equator's position. As illustrated in Figure 5.4, Polarization are oriented along the x axis when $S_1 > 0$, whereas, conversely, polarization is directed along the y axis if $S_1 < 0$. In contrast, the polarization is $+45^0$ if $S_2 > 0$ and -45^0 if $S_2 < 0$. Right-circular polarization corresponds to the North Pole and left-circular polarization corresponds to the South Pole. It can be observed in Figure 5.4 all circular and elliptical polarizations rotate clockwise in the northern hemisphere, whereas in the southern hemisphere the rotations are counterclockwise. Using the (ε, θ) and (ψ, Δ) coordinate systems, it is possible to describe any point on the Poincare sphere surface as shown in Figure 5.5.

The coordinates of the elliptical polarization are determined by the main axis (distance $2a$) and small axis (distance $2b$) in the (ε, θ) system.

Major axis angle in relation to E_x direction is known as the azimuth θ, however, ε is the representation of ellipticity angle as given by $\tan\varepsilon = b/a$. If $\tan\varepsilon = 0$, the type of polarization will become linear polarization. On the Poincar sphere equator, the only theta will be changed with $\varepsilon = 0$. Alternatively, when the latitude is varied from an equator-fixed position with a constant θ, only ε changes.

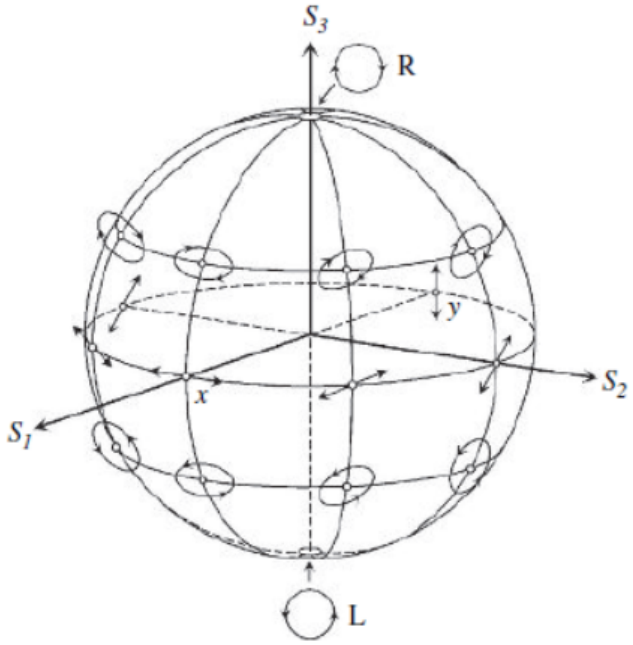

Figure 5.4: Polarization represented by the Poincar sphere[100].

The two angles (ε, θ) that appear in figure 5.5 (a) represent the polarization state in the (ε, θ) coordinate system. As can be seen in Figure 5.6, the point $P(S_1S_2S_3)$ on the Poincar sphere surface is given by [100]:

$$S_1 = \cos 2\varepsilon \cos 2\theta \tag{5.5}$$

$$S_2 = \cos 2\varepsilon \sin 2\theta \tag{5.6}$$

$$S_3 = \sin 2\varepsilon \tag{5.7}$$

It can be seen from Equations (5.5-6) that the values of S_1 and S_2 are derived from the value of 2ε. As a result, there is no difference between the lower and upper sides of polarized light and one complete rotation of 180^0 degrees is equivalent to one complete rotation of the optical axis. Furthermore, the value of 2ε in Equations (5.5-6) arises from the fact that at $\varepsilon = 45^0$, $a = b$. Using Equations (5.5-6), (ε, θ) values can be calculated from Stokes parameters as follows:

$$\theta = \frac{1}{2}\tan^{-1}(\frac{S_2}{S_1}) \tag{5.8}$$

$$\varepsilon = \frac{1}{2}\sin^{-1}(S_3) \tag{5.9}$$

In figure 5.3, the angles (psi, delta) correspond to the amplitude ratio($\tan\psi = E_{x0}/E_{y0}$) and phase difference($\Delta = \delta_x - \delta_y$), respectively.

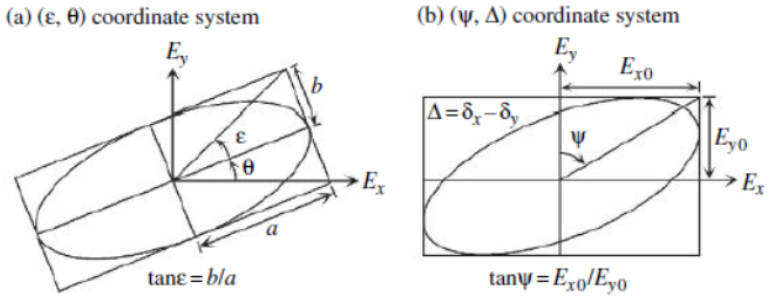

Figure 5.5: An elliptical polarization representation by the (ε, θ) system (a) and (ψ, Δ) coordinate system (b) [100]

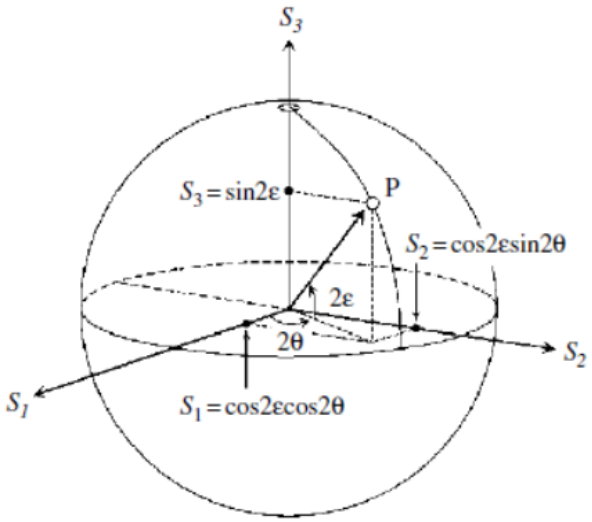

Figure 5.6: (ε, θ) coordinates are used to represent a point P on the Poincar sphere surface [100] .

5.6 Stokes Parameters

The Stokes parameters will be used to analyze the measurement and determine the ellipsometry angles (ψ, Δ). The Stokes vector (parameters) employed to determine the polarization of light. All polarization types and even partially or unpolarized light can be described using Stokes parameters. Stokes parameters are measured in actual ellipsometry measurements. Stokes parameters can be described in a number of different ways.

In ellipsometry measurements we fit the data to evaluate the Stokes parameters, these parameters are then used to calculate ellipsometery angles (ψ, Δ). When using the polarized light intensity, Stokes' parameters (S_{0-3}) can be expressed as follows [100]:

$$S_0 = I_x + I_y \tag{5.10}$$

$$S_1 = I_x - I_y \tag{5.11}$$

$$S_2 = I_{+45} - I_{-45} \tag{5.12}$$

$$S_3 = I_R - I_L \tag{5.13}$$

Here, S_0 is the total intensity of light and S_1 displays the light intensity obtained by deducting the linear polarization light intensity in the y direction (I_y) from intensity that in the x direction (I_x). However, S_2 is the intensity of light calculated by deducting the linear polarization light intensity in -45^0 (I_{-45}) from linear polarization intensity at $+45^0$ (I_{+45}). In relation to the parameter S_3, the intensity of light of the left-circular polarization (I_L) is reduced from intensity of right-circular polarization (I_R). Therefore, the parameters (S_{1-3}) indicate the differences in the intensity of light between each state of polarization as it shows in Figure 5.7.

The stokes parameters S_1,S_2 and S_3 are basically what we measure in our experiments. By using Stokes parameters derived from Poincar spheres, we can calculate the ellipsometry angles as following:

$$S_1 = -\cos 2\psi \tag{5.14}$$

$$S_2 = \sin 2\psi cos\Delta \tag{5.15}$$

$$S_3 = -\sin 2\psi \sin \Delta \tag{5.16}$$

To calculate the complex refractive index, we will use the ellipsometry angles, which are calculated from the Stokes parameters. Figure 5.8 illustrates the basic setup for calculating the refractive index.

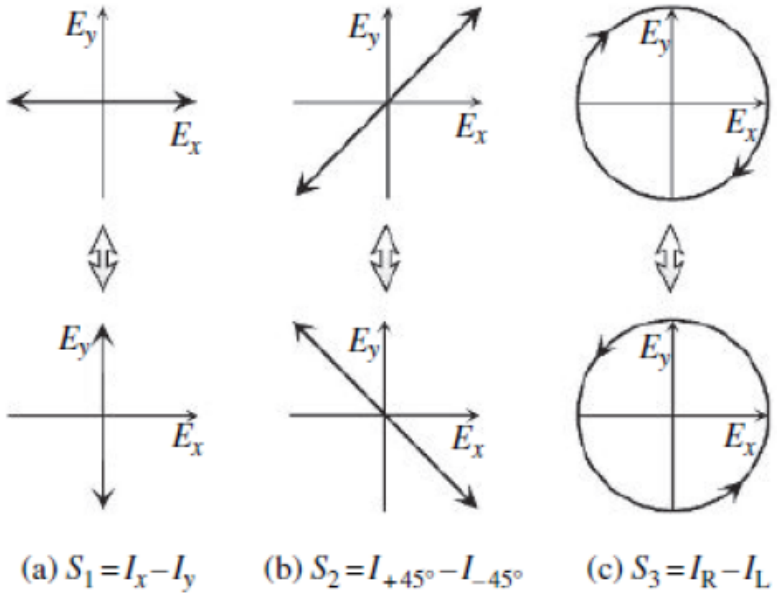

Figure 5.7: Stokes parameters with respect to light intensity [100].

Where the θ_0 represents the incident angle and θ_1 represents the transmission angle. Based on Frensel reflection coefficients for r_s and r_p we obtain the following equations [105].

$$r_p = \frac{\tilde{n}_1 cos(\theta_0) - \tilde{n}_0 cos(\theta_1)}{\tilde{n}_1 cos(\theta_0) + \tilde{n}_0 cos(\theta_1)} \tag{5.17}$$

$$r_s = \frac{\tilde{n}_0 \cos(\theta_0) - \tilde{n}_0 \cos(\theta_1)}{\tilde{n}_0 \cos(\theta_0) + \tilde{n}_1 \cos(\theta_1)} \tag{5.18}$$

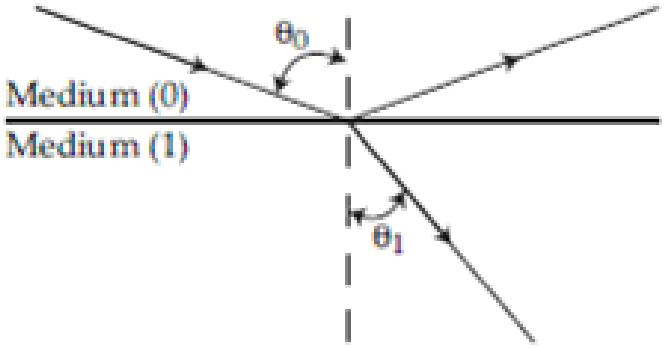

Figure 5.8: Light waves that are reflected and transmitted at a surface interface.

In this case, $\cos\theta_1$ can be calculated via Snell's law as follows:

$$\tilde{n}_0 \cos\theta_0 = \tilde{n}_1 \cos\theta_1 \tag{5.19}$$

$$\sin^2\theta + \cos^2\theta = 1 \tag{5.20}$$

$$\tilde{n}_1 \cos(\theta_1) = (\tilde{n}_1^2 - \tilde{n}_0^2 \sin^2\theta_0)^{\frac{1}{2}} \tag{5.21}$$

$$cos(\theta_1) = \sqrt{1 - (\frac{\tilde{n}_0}{\tilde{n}_1}) sin^2(\theta_0)} \tag{5.22}$$

Her $\tilde{n}_0$,$\tilde{n}_1$ the refractive index of the first medium (air) and second medium respectively, while θ_0 is the incident angle and θ_1 is the refractive angle. To calculate the complex

refractive index $\tilde{n}$, we inserting (5.17), (5.18) and (5.22) into (5.3) and solve it for $\tilde{n}$

$$\tilde{n}_1 = \frac{[\sqrt{1 - 4sin^2(\theta_0)tan(\psi)e^{j\delta} + 2tan(\psi)e^{j\delta} + tan^2(\psi)e^{e\delta}}]\tilde{n}_0 sin(\theta_0)}{cos(\theta_0[1 + tan(\psi)e^{j\delta}]} \tag{5.23}$$

5.7 Ellipsometry Measurement

Prior to the 1970s, only null ellipsometry instruments were employed for measurements [106]. However, this type of ellipsometer is no longer commonly used, with the exception of imaging ellipsometry, which measures in two dimensions [107, 108, 109]. Instruments for spectroscopic ellipsometry currently in use can be divided into two main categories: rotating optical elements [110, 111] and photoelastic modulation instruments [112, 113]. An ellipsometer with rotating elements can be further divided into rotating-analyzer ellipsometry (RAE) [114, 115] and rotating-compensator ellipsometry (RCE) [116]. However, it is only recently spectroscopic ellipsometry measurements have been applied to infrared wavelengths [117, 118, 119]. In this study, we used rotating analyzer ellipsometry. The ellipsometry with rotating optical elements will be described in the following sections.

5.8 Rotating-Analyzer Ellipsometry

A rotating analyzer ellipsometry is described by PSA_R, where P, S, and A represent the polarizer, sample, and analyzer, respectively. The addition of the subscript to A shows that the analyzer is continuously rotating. The arrangement is described in Figure 5.9 including a light source (laser) and polarizer at the side of the incidence, and an analyzer with a detector on the side of the reflection.

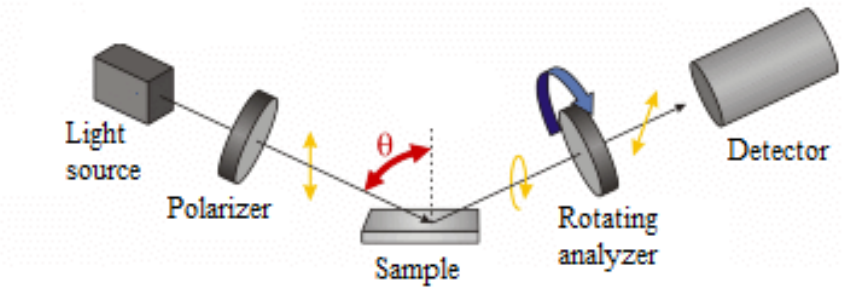

Figure 5.9: The set-up of rotating analyzer ellipsometry, where the linear polarizer is placed on the incident side while the rotating analyzer is placed on the reflected side.

The figure 5.10 illustrates the polarization patterns of the p-polarized and the s-polarized light reflected by surfaces, where the p-polarized light is parallel to the incident plane and the s-polarized is normal to the incident plane.

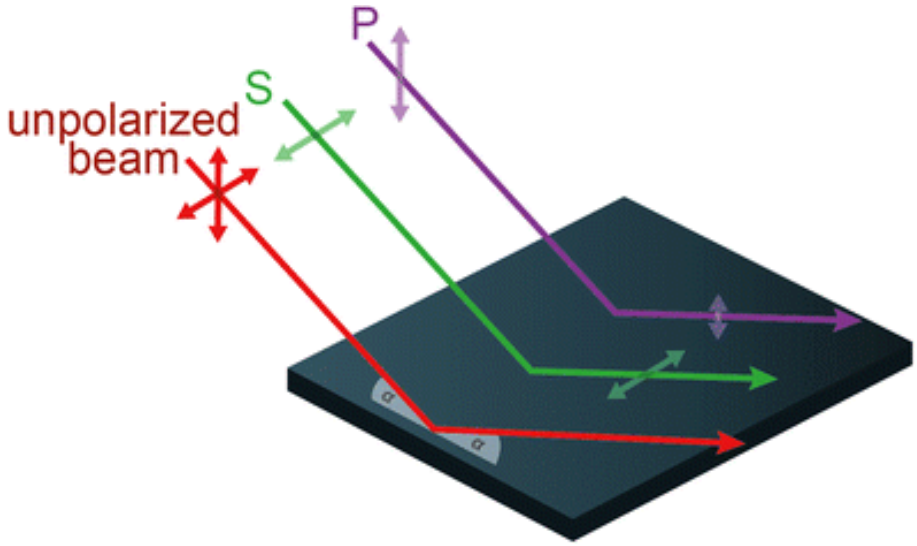

Figure 5.10: P and s-polarized light reflected from a surface.

Since the ellisometry measurements depend on the reflection p-polarize and s-polarize amplitude ratio, the incident angle should be set at Brewster angel, where the maximum difference between p-polarization and s-polarization is occurring. The two polarized components reflected from the surface of the sample and passed through the rotating analyzer. As the polarized light passes through the rotating analyzer, the detector will indicate the intensity of the polarized light at different rotating analyzer angles.

The following equations are used to obtain the light intensity measured by the detector [100]:

$$I = |E_A|^2 \tag{5.24}$$

$$I = I_0(1 - cos2\psi \cos 2A + \sin 2\psi \cos \Delta \sin 2A) \tag{5.25}$$

$$= I_0(1 + S_1 \cos 2A + S_2 \sin 2A) \tag{5.26}$$

In this case, E_A is the electric field as a function of analyzer angle, I_0 is the intensity of incident light, A is the angle of the analyzer and $S1$,$S2$ are Stokes parameters.

One of the main advantages of rotating analyzer ellipsometry is its simplicity of optical configuration in comparison to other ellipsometry configurations. The disadvantage of this method, however, is an increase in error measurements when Δ at 0^0 and 180^0

5.9 Rotating Analyzer Ellipsometry with Compensator

As mentioned above in RAE, the measurement error is increased when Δ at 0^0 and 180^0. In addition, the Stokes parameter S_3 cannot be measured. In order to overcome these problems, introducing a compensator into the RAE can help to resolve the problem. Because of this, there has been an increase in the popularity of RAE with a compensator over the past ten years.

Figure 5.11 shows Rotating-Analyzer Ellipsometry with Compensator, ($RACE$). The advantage of this ellipsometry configuration is it is capable of determining all (ψ,Δ), and even depolarization spectrum can be measured. Furthermore, the method is uniformly sensitive to (ψ,Δ) measurement. As a disadvantage, in this method a longer data acquisition time is required compared to PSA_R and the optical configuration is more complex.

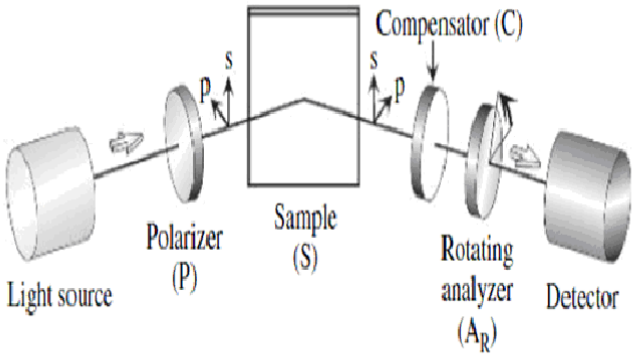

Figure 5.11: The set-up of rotating analyzer ellipsometry with compensator, where the linear polarizer is placed on the incident side while the compensator and rotating analyzer are placed on the reflected side.

To determine the intensity of the light measured by the detector, the following formulas are applied [100]:

$$I = I_0[1 - \cos 2\psi \cos 2A + \sin 2\psi \cos(\Delta - \delta) \sin 2A] \tag{5.27}$$

$$= I_0[1 - \cos 2\psi \cos 2A + (\sin 2\psi \cos \Delta \cos \delta + \sin 2\psi \sin \Delta \sin \delta) \sin 2A] \tag{5.28}$$

$$= I_0[1 + S_1 \cos 2A + (S_2 \cos \delta - S_3 \sin \delta) \sin 2A] \tag{5.29}$$

Due to the compensator in this configuration, Δ is shifted while ψ was not affected. In another word the p-polarization and s-polarization amplitude values do not change by compensator. In fact, it is only the phase difference that changes with the compensator. Accordingly, the phase difference introduced by the compensator can be described by replace Δ by Δ^- where $\Delta^- = \Delta - \delta, \delta$ represents the added phase generated by the compensator. .

5.10 Rotating-Compensator Ellipsometry (RCE)

In this configuration, the compensater rotates while the optical axes of the polarizer and analyzer are oriented 45^0 with respect to each other as it shows in Figure 5.12.

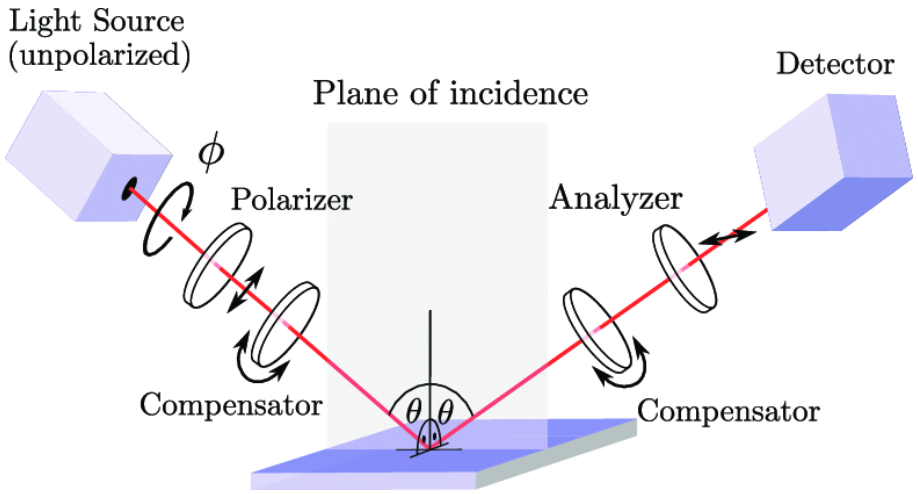

Figure 5.12: The set-up of rotating compensator ellipsometry, where the linear polarizer and rotating compensator are placed on the incident or reflected side while the analyzer is placed on the reflected side.

Figure 3-5 shows that the rotating compensator can be placed either before or after the sample. The light intensity detected by a detector is obtained as follows [100].

$$I = |E_A|^2 \tag{5.30}$$

$$I = I_0(2 - \cos 2\psi + 2\sin 2\psi \sin\Delta \sin 2C - \cos 2\psi \cos 4C + \sin 2\psi \cos\Delta \sin 4C) \tag{5.31}$$

$$= I_0(2 + S_1 - 2S_3 \sin 2C + S_1 \cos 4C + S_2 \sin 4C) \tag{5.32}$$

Here C is the compensator angle.

In comparison to the rotating analyzer ellipsometry, the alignment of the rotating compensator ellipsometry is more complicated, which is one of its disadvantages. While the main benefit of using a rotating compensator is it can calculate all (ψ, Δ).

5.11 Ellipsometry Set-Up

To develop accurate measurements of the time resolved ellipsometry , we conducted calibration tests with samples having well-known optical parameters . The work involved building a rotating analyzer ellipsometry set-up using a 10μm p-polarized laser as a source and two linear polarizers covering a 10-12 μm spectrum. An infrared p-polarized laser beam passes through the first linear polarizer, rotated at a 45^0 with respect to the incident plan. The linear polarizer passes through s- and p-polarized light with the same amplitudes and no phase difference which is an essential condition to perform ellipsometry measurements. Both s-polarized light and p-polarized light are guided to the sample with an incident angle equal to Brewster's angle. We calibrated our measurements using Germanium(Ge) and Silicon(Si), which have well-known refractive index. The Brewster angle is calculated as 75^0 at 10μm wavelength for Ge and 76^0 for (Si). Light reflecting from the sample passes through another linear polarizer (analyzer) that is rotated by a motorized stage with a 2^0 resolution. The reflected light is then collimated by the lens towards the detector in order to measure the intensity as a function of analyzer angle. To calculate Stocks parameters S_1 and S_2, the collimated data has been fitted using equation 5.26. In the next step, the ellipsometry parameters ψ and Δ were calculated by applying equations 5.14 and 5.15 respectively. A refractive index was then calculated using equation 5.23 for each sample. According to the literature, the results were consistent within the boundaries of $(N = (n \pm 0.2) + (k \pm 0.03)i)$, which indicates that the calibration of the ellipsometry setup was successful.

5.12 Time Resolved Ellipsometry

This section presents the results of home-made time-resolved ellipsometry measurements. In contrast to the intrinsic uncertainty of time-resolved reflectometery measurements, where only amplitude changes of reflectance can be measured as a result of probe delay, the measurements of time-resolved eellipsometry provide for complete estimation of complex

refractive indexes over time $N(t) = n(t) - ik(t)$.

The motivation of the measurements is to investigate the change in electro-optical properties of the TI sample following excitation of the sample surface. A visible pump at 800 nm and an IR probe at 4 μm were used in this study to conduct the measurements. The advantages of using an IR probe is that the probe energy ensures that interband excitation is not induced. Figure 5.13 shows the home-made time resolved ellipsometry set-up.

As far as we are aware, there are no publications in the literature referring to the study of optical surface properties of TI using time-resolved ellipsometry. Perhaps this is the first study to use pump-probe ellipsometry to observe how the optical index of TI surfaces changes following excitation in the far IR. To conduct this work, a rotating analyzer ellipsometer as shown in Figure 5.9 was constructed.

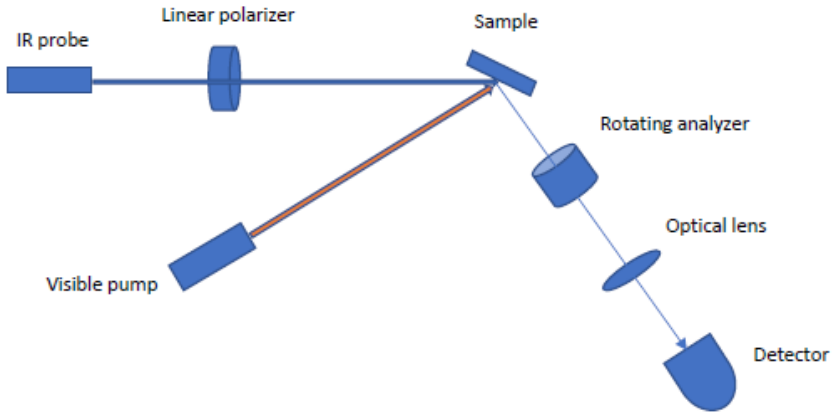

Figure 5.13: Schematic illustration Time-resolved ellipsometry with rotating analyzer configuration.

In this work, two linear polarizers were used covering a spectrum range of (4-6)μm. One of these polarizers is rotated at 45^0 with respect to the incident plan in the probe arm to specify the initial polarization.

5.13 Results

Time resolved ellipsometry measurements were performed using a coherent ultrafast laser system described in chapter 2. The photo in 5.14 illustrates the set-up of home-made ellipsometry which pointed the path of the pump and probe with optical elements. The time-resolved rotating analyzer ellipsomerty was performed with a 2 ps time delay between pump and probe. To put it another way, the ellipsometry measurements were performed every 2 ps. Ellipsometry measurements began at the negative delay time -4 ps (before the pump arrives) and continued until the excited carriers had relaxed 12 ps. The reflectance intensity was fitted using equation 4.26 to calculate the Stokes parameters S_1 and S_2. MATLAB was used to fit the data in this work. The figure 5.15 illustrates the reflectance intensity measured over a 360^0 rotation analyzer at zero probe delay, while figure 5.16 and 5.17 show the fitting with different probe delays, ranging from -4 ps to 12 ps.

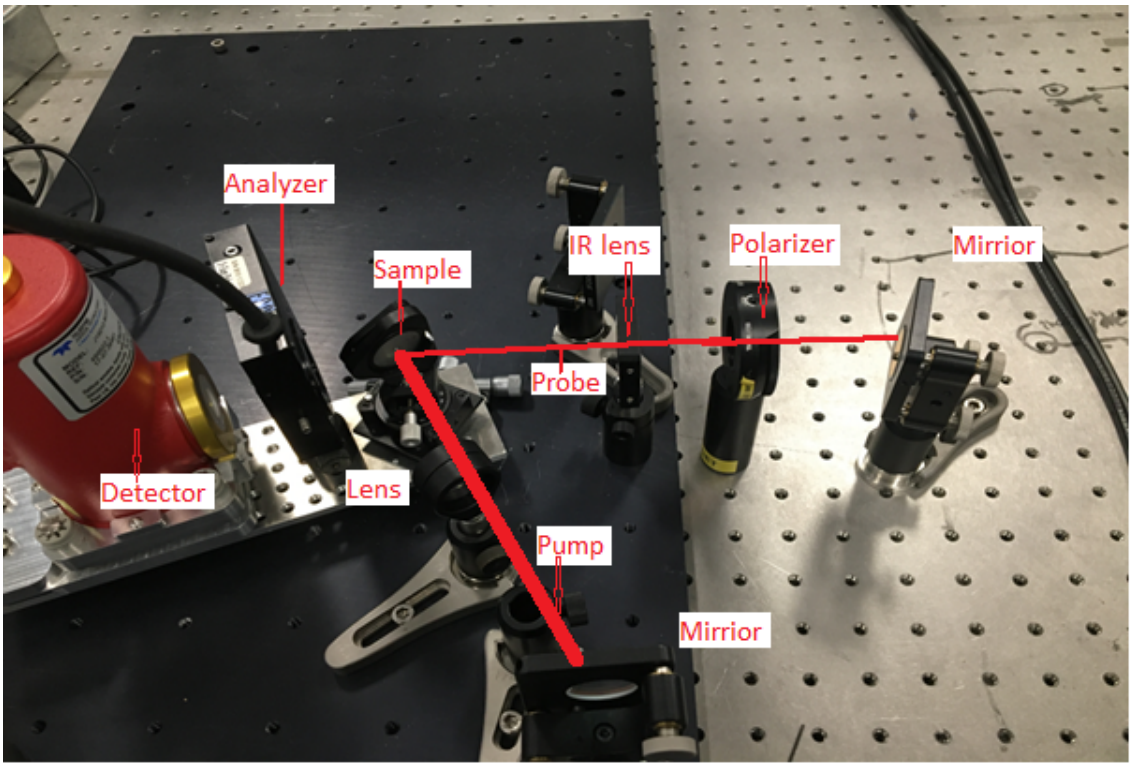

Figure 5.14: Display of the polarizer, sample, analyzer, and detector in an ellipsometry set-up.

After calculating the stock parameters S_1, S_2, equations 5.14 and 5.15 were used to

estimate the ellipsometry coefficients ψ and Δ.

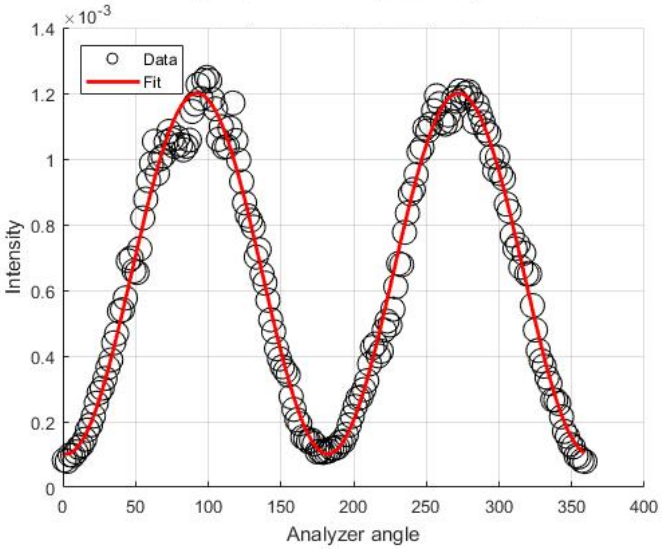

Figure 5.15: Reflectance signal from the sample surface as a function of the rotated analyzer's angle at zero probe delay.

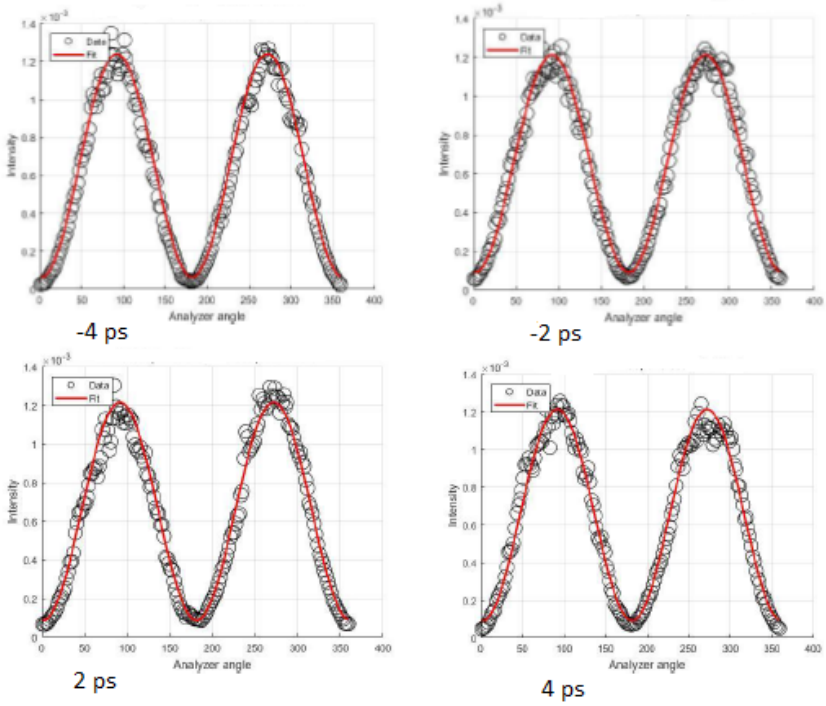

Figure 5.16: Present Reflectance signal from the sample surface as a function of the rotated analyzer's angle at different delay times -4 ps, -2 ps, 2 ps, 4 ps.

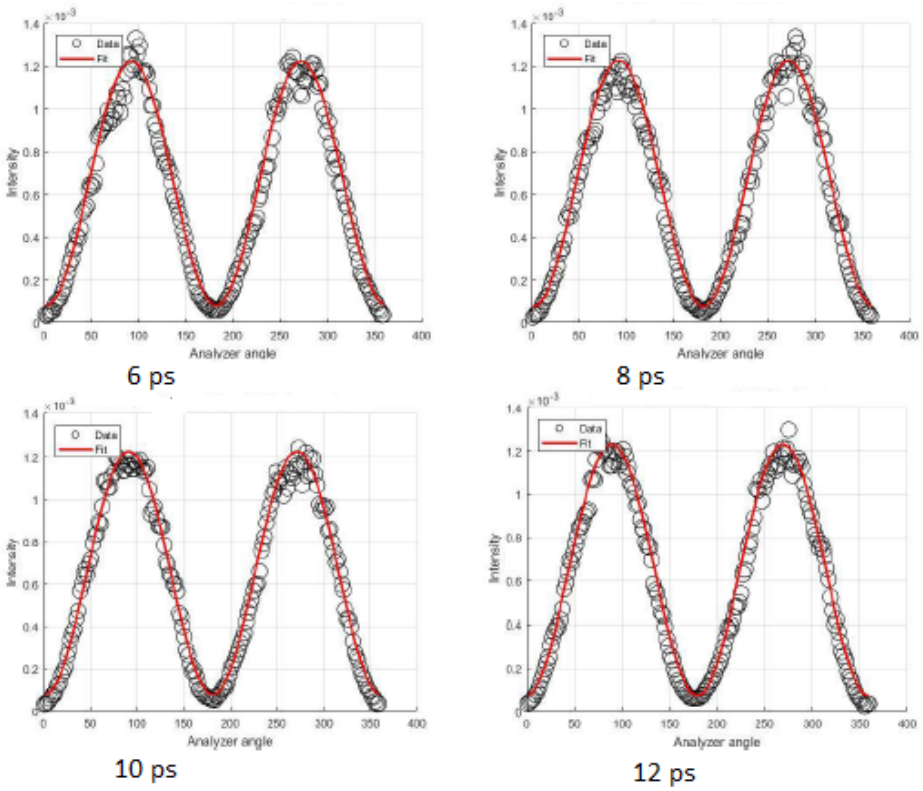

Figure 5.17: Reflectance signal from the sample surface as a function of the rotated analyzer's angle at different delay times 6 ps, 8 ps, 10 ps, 12 ps.

Figure 5.18 illustrates the comparison between laser intensity measurements without sample and laser intensity measurements reflected from samples over 360^0 analyzer. The purpose of these measurements is to ensure that the laser polarization state does not change when reflected from the sample.

Figure 5.19 illustrates the intensity of the reflectance probe before, at zero, and following zero delay according to analyzer angle.

Figure 5.20 shows the values of ellipsometry parameters (ψ) and (Δ) as a function of the probe delay. As can be seen in figure 5.20, ψ and Δ increase significantly around zero delay. As the delay time between the pump and probe increases, both ψ and Δ decrease. The complex refractive index was calculated using equation 5.23 where applying the Brewster angle (Θ) , ψ and Δ for each probe delay. Figure 4.21 shows that the real and imaginary parts of the complex refractive index of the surface were calculated

based on measurement results. Following the excitation, the refractive index n of the surface decreased to a minimum value, while the extinction coefficient k increased to its maximum value. The values of n and k were returned to their original values within a few picoseconds.

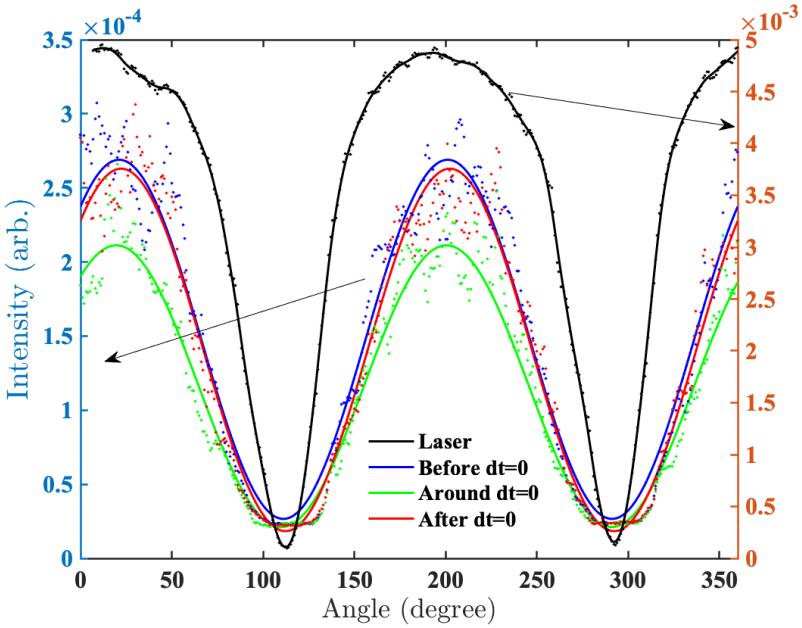

Figure 5.18: Intensity of the laser without and with a sample as a function of the analyzer angle.

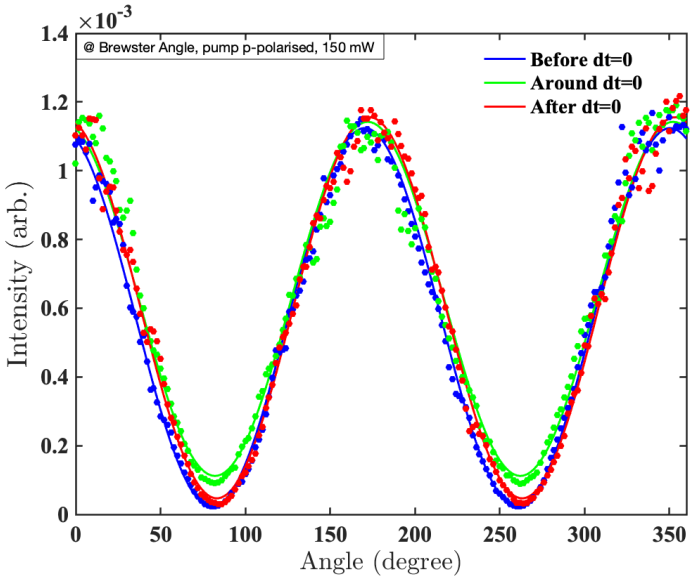

Figure 5.19: Scheme illustration Time-resolved ellipsometry with rotating analyzer configuration.

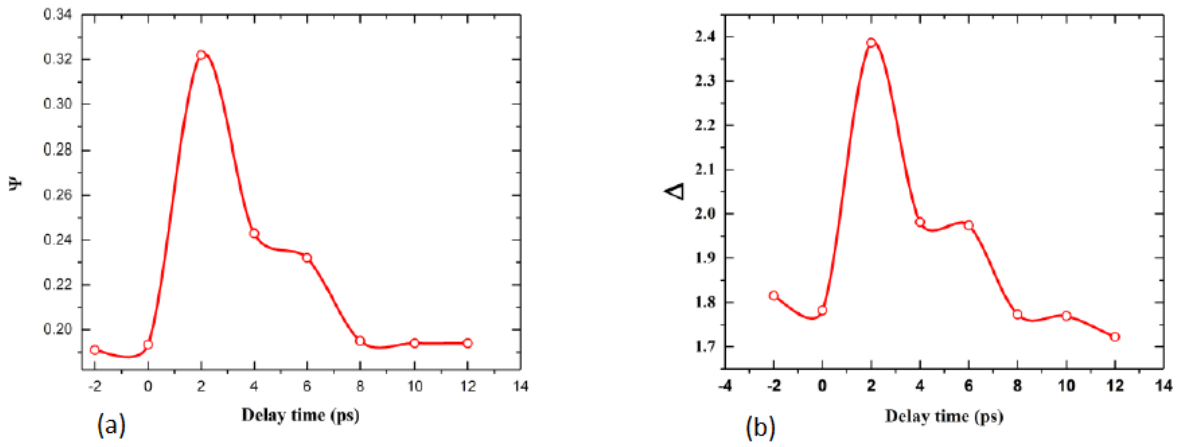

Figure 5.20: Ellipsometry parameters (a) ψ and (b) Δ as functions of probe delay at Brewster angle.

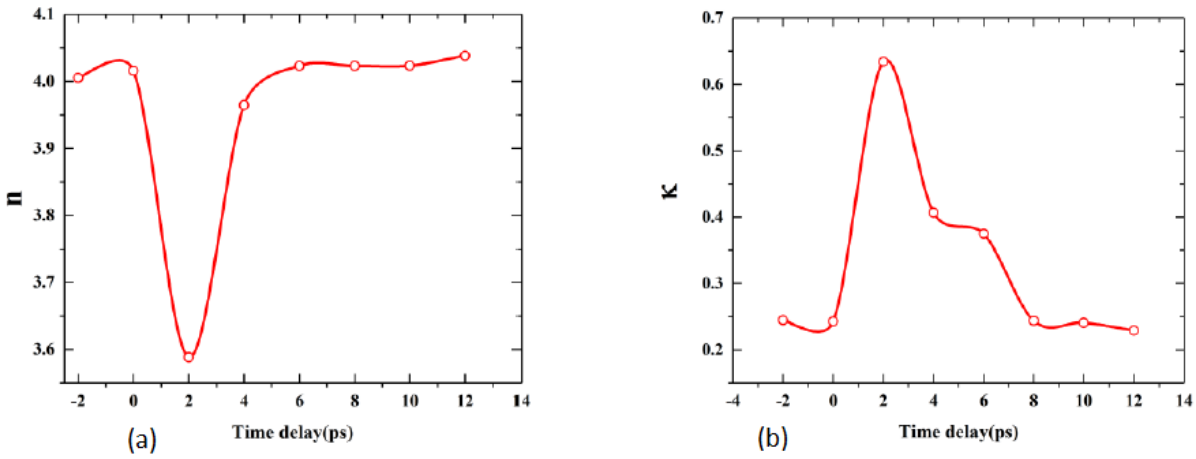

Figure 5.21: (a) Real part of the refractive index n and (b) extinction coefficient k as a function of the probe delay at Brewster angle.

5.14 Discussion

The aim of this study was to determine how the optical parameters of the sample surface changed following the excitation of the sample surface using time-resolved ellipsometry. Optical constants are fundamental properties of materials that determine the interaction between incident light and the material. There are two components of the refractive index: real and imaginary, which can be given according to the following relationship:

$\varepsilon = \varepsilon_1 + i\varepsilon_2 = (n + ik)^2$

In this case ε represents the complex dielectric function, n the refractive index, ε_1 and ε_2 the real and imaginary part of the dielectric function, and n, k represent the real part of the refractive index and the imaginary part (extinction coefficient) respectively.

Using a spectroscopic time resolved ellipsometer, we measured the n and k values for cleaved flat Bi_2Te_3 single crystal by using equation 5.23. Figure 5.21 illustrates the relationship between n and k of the sample surface as a function of the probe delay.

According to our measurements, it was found that after reaching zero delay, the n drops significantly to reach the minimum value, then gradually recovers. On the other hand, the k increased following zero delay due to the induction of free carriers on the surface. Previous studies have shown that when TI carriers are excited by a femtosecond laser, these hot carriers emit coherent phonons which relax within the conduction band. These phonons change the optical properties of the surface, resulting in changing the refractive index [12, 120, 121].

The pump pulses in the visible spectrum, generating free carriers that oscillate on the surface of the sample. The IR probe absorption increases rapidly following excitation due to the generation of free carriers on the surface. The scattering of free carriers on the surface led to a damping of carriers oscillation and the recovery of k within a few picoseconds. Our results were in agreement with the Drude model which predicted that increasing concentration of carriers would lead to increasing k while n decreases [122, 100].

CHAPTER 6

CONCLUSION AND FUTURE WORKS

6.1 Conclusion

This thesis presents work on opto-electronic characteristics and the dynamics of free carriers in TI. Measurements of the excited state properties of the samples were conducted using the femtosecond pump-probe technique combined with probing and excitation dependence of the polarization states.

The results show the generation of surface plasma waves following the excitation by the pump. We measured pump polarization dependence and pump power dependence. With a p-polarized pump, the reflectance change $\frac{\Delta R}{R_0}$ signal shows strong response, whereas with an s-polarized pump, the signal remains unchanged. This is a clear demonstration of the surface wave in TI. Additional measurements included pump power dependence as a function of the probe delay. The results showed that the $\frac{\Delta R}{R_0}$ signals increased as pump power increased and more free carriers are excited. Surprisingly, the decay time of plasma waves increased with pump fluence. We speculate that the increase in decay time is because the available phase space for scattering in the Dirac cone becomes smaller with higher fluence. In chapter 4 we presented the development of home-made time-resolved ellipsometry measurements. This experiment was designed to investigate the change of complex refractive index of the sample surface response to the excitation. The results showed the real part, n decreases, while the imaginary part, k increases with increasing

the number of carriers on the surface by excitation which is in line with the Drude model.

The results show that Bi_2Te_3 has a high refractive index in the IR region. The measurements indicate that the refractive index of the surface can be highly tunable. Bi_2Te_3 exhibit a number of novel electrical and optical features that make it extremely attractive as electronic, and optoelectronic materials in the infrared region. Therefore, in order to efficiently control light and enhance the performance of optical devices, it would be ideal to combine the excellent properties of metallic surfaces with ultrafast plasmonic properties and a highly tunable refractive index.

6.2 The future works

Based on the results of this study, it can be concluded that the possibility to generate ultrafast surface plasma on the surface of TI. We found that pump fluence could be used to control the decay time of the surface wave. It may be worthwhile to investigate in more detail the properties of the surface wave and its decay time dependence. Hence, the following proposals have been made in order to guide the future development of this research. As a first step, it is necessary to develop an experiment to investigate how pump wavelength affects plasma wave decay time, as well as probe dependence. It will then be possible to determine whether the surface wave can be controlled by pumping or probing wavelengths. In addition, it will be possible to determine the ideal wavelength to generate and control the plasma wave.

A second factor that may be helpful in understanding surface wave generation on the TI surface is the thickness dependence of the sample. The exfoliation technique was unable to control the thickness of the sample, which was one of the difficulties we encountered.

In time resolved ellipsometry, using a single wavelength pump and probe, we investigated the complex refractive index. We recommend using wide spectrum pump-probe ellipsometry in order to gain a better understanding of the electro-optical properties of the TI surface.

LIST OF REFERENCES

[1] Park Benjamin. *A history of electricity:(The intellectual rise in electricity) from antiquity to the days of Benjamin Franklin*. J. Wiley & Sons, 1895.

[2] Stephen Gray. Stephen gray (scientist).

[3] K v Klitzing, Gerhard Dorda, and Michael Pepper. New method for high-accuracy determination of the fine-structure constant based on quantized hall resistance. *Physical review letters*, 45(6):494, 1980.

[4] DJ Thouless, Mahito Kohmoto, MP Nightingale, and M Den Nijs. Quantized hall conductance in a two-dimensional periodic potential. *Physical Review Letters*, 49(6):405, 1982.

[5] F Duncan M Haldane. Model for a quantum hall effect without landau levels: Condensed-matter realization of the" parity anomaly". *Physical review letters*, 61(18):2015, 1988.

[6] Shuichi Murakami, Naoto Nagaosa, and Shou-Cheng Zhang. Dissipationless quantum spin current at room temperature. *Science*, 301(5638):1348–1351, 2003.

[7] Charles L Kane and Eugene J Mele. Quantum spin hall effect in graphene. *Physical review letters*, 95(22):226801, 2005.

[8] J. E. Moore and L. Balents. Topological invariants of time-reversal-invariant band structures. *Phys. Rev. B*, 75:121306, Mar 2007.

[9] Yuqi Xia, Dong Qian, David Hsieh, L Wray, Arijeet Pal, Hsin Lin, Arun Bansil, DHYS Grauer, Yew San Hor, Robert Joseph Cava, et al. Observation of a large-gap topological-insulator class with a single dirac cone on the surface. *Nature physics*, 5(6):398–402, 2009.

[10] Nardeep Kumar, Brian A Ruzicka, NP Butch, P Syers, K Kirshenbaum, J Paglione, and Hui Zhao. Spatially resolved femtosecond pump-probe study of topological insulator bi 2 se 3. *Physical Review B*, 83(23):235306, 2011.

[11] Jianbo Hu, Kyushiro Igarashi, Takao Sasagawa, Kazutaka G Nakamura, and Oleg V Misochko. Femtosecond study of a1g phonons in the strong 3d topological insulators: From pump-probe to coherent control. *Applied Physics Letters*, 112(3):031901, 2018.

[12] Qiya Liu, Ruihui Shao, Ning Li, Weizheng Liang, Xinsheng Yang, SN Luo, and Yong Zhao. Anharmonicity of bi2se3 revealed by fs transient optical spectroscopy. *Applied Physics Letters*, 115(20):201902, 2019.

[13] Richarj Mondal, Akira Arai, Yuta Saito, Paul Fons, Alexander V Kolobov, Junji Tominaga, and Muneaki Hase. Coherent dirac plasmons in topological insulators. *Physical review B*, 97(14):144306, 2018.

[14] Yuri D Glinka, Sercan Babakiray, Trent A Johnson, Alan D Bristow, Mikel B Holcomb, and David Lederman. Ultrafast carrier dynamics in thin-films of the topological insulator bi2se3. *Applied Physics Letters*, 103(15):151903, 2013.

[15] Chih-Wei Luo, H-J Chen, HJ Wang, SA Ku, Kaung-Hsiung Wu, TM Uen, Jenh-Yih Juang, J-Y Lin, Ben-Li Young, T Kobayashi, et al. Ultrafast dynamics in topological insulators. In *Ultrafast Phenomena and Nanophotonics XVII*, volume 8623, pages 59–65. SPIE, 2013.

[16] Sunghun Kim, Mao Ye, Kenta Kuroda, Yohei Yamada, EE Krasovskii, EV Chulkov, Koji Miyamoto, Masashi Nakatake, Taichi Okuda, Yoshifumi Ueda, et al. Surface scattering via bulk continuum states in the 3d topological insulator bi 2 se 3. *Physical Review Letters*, 107(5):056803, 2011.

[17] Tong Zhang, Peng Cheng, Xi Chen, Jin-Feng Jia, Xucun Ma, Ke He, Lili Wang, Haijun Zhang, Xi Dai, Zhong Fang, et al. Experimental demonstration of topological surface states protected by time-reversal symmetry. *Physical Review Letters*, 103(26):266803, 2009.

[18] Zhanybek Alpichshev, JG Analytis, J-H Chu, Ian R Fisher, YL Chen, Zhi-Xun Shen, Alan Fang, and Aharon Kapitulnik. Stm imaging of electronic waves on the surface of bi 2 te 3: topologically protected surface states and hexagonal warping effects. *Physical review letters*, 104(1):016401, 2010.

[19] Pedram Roushan, Jungpil Seo, Colin V Parker, Yew San Hor, David Hsieh, Dong Qian, Anthony Richardella, M Zahid Hasan, Robert Joseph Cava, and Ali Yazdani. Topological surface states protected from backscattering by chiral spin texture. *Nature*, 460(7259):1106–1109, 2009.

[20] YL Chen, James G Analytis, J-H Chu, ZK Liu, S-K Mo, Xiao-Liang Qi, HJ Zhang, DH Lu, Xi Dai, Zhong Fang, et al. Experimental realization of a three-dimensional topological insulator, bi2te3. *science*, 325(5937):178–181, 2009.

[21] David Hsieh, Yuqi Xia, Dong Qian, L Wray, Fabian Meier, Jurg Osterwalder, Luc Patthey, Joseph G Checkelsky, NP Ong, Alexei V Fedorov, et al. A tunable topological insulator in the spin helical dirac transport regime. *Nature*, 460(7259):1101–1105, 2009.

[22] AA Taskin, Satoshi Sasaki, Kouji Segawa, and Yoichi Ando. Manifestation of topological protection in transport properties of epitaxial bi 2 se 3 thin films. *Physical review letters*, 109(6):066803, 2012.

[23] JG Checkelsky, YS Hor, RJ Cava, and NP Ong. Bulk band gap and surface state conduction observed in voltage-tuned crystals of the topological insulator bi 2 se 3. *Physical review letters*, 106(19):196801, 2011.

[24] Hadar Steinberg, Dillon R Gardner, Young S Lee, and Pablo Jarillo-Herrero. Surface state transport and ambipolar electric field effect in bi2se3 nanodevices. *Nano letters*, 10(12):5032–5036, 2010.

[25] SK Sundaram and Eric Mazur. Inducing and probing non-thermal transitions in semiconductors using femtosecond laser pulses. *Nature materials*, 1(4):217–224, 2002.

[26] JA Fleck Jr. Ultrashort-pulse generation by q-switched lasers. *Physical Review B*, 1(1):84, 1970.

[27] G Steinmeyer, DH Sutter, L Gallmann, N Matuschek, and U Keller. Frontiers in ultrashort pulse generation: pushing the limits in linear and nonlinear optics. *Science*, 286(5444):1507–1512, 1999.

[28] Arthur J Nozik. Nanoscience and nanostructures for photovoltaics and solar fuels. *Nano letters*, 10(8):2735–2741, 2010.

[29] Charles Smith and David Binks. Multiple exciton generation in colloidal nanocrystals. *Nanomaterials*, 4(1):19–45, 2013.

[30] Francesco Priolo, Tom Gregorkiewicz, Matteo Galli, and Thomas F Krauss. Silicon nanostructures for photonics and photovoltaics. *Nature nanotechnology*, 9(1):19–32, 2014.

[31] Kian-Giap Gan, Chi-Kuang Sun, Steven P DenBaars, and John E Bowers. Ultrafast valence intersubband hole relaxation in ingan multiple-quantum-well laser diodes. *Applied physics letters*, 84(23):4675–4677, 2004.

[32] Kristopher W Williams, Nicholas R Monahan, Daniel D Koleske, Mary H Crawford, and X-Y Zhu. Ultrafast and band-selective auger recombination in ingan quantum wells. *Applied Physics Letters*, 108(14):141105, 2016.

[33] Ammar Zakar, Rihan Wu, Dimitri Chekulaev, Vera Zerova, Wei He, Leigh Canham, and Andrey Kaplan. Carrier dynamics and surface vibration-assisted auger recombination in porous silicon. *Physical Review B*, 97(15):155203, 2018.

[34] Uditendu Mukhopadhyay, Dipanjan Chaudhuri, Jit Sarkar, Sourabh Singh, Radha Krishna Gopal, Sandeep Tammu, Prashanth C Upadhya, and Chiranjib Mitra. Surface optical and bulk acoustic phonons in the topological insulator, bi2se2te. *Applied Physics Letters*, 106(24):241106, 2015.

[35] Mahdi Hajlaoui, E Papalazarou, Julien Mauchain, G Lantz, N Moisan, Davide Boschetto, Z Jiang, I Miotkowski, YP Chen, A Taleb-Ibrahimi, et al. Ultrafast surface carrier dynamics in the topological insulator bi2te3. *Nano letters*, 12(7):3532–3536, 2012.

[36] Encyclopaedia Britannica. Available online: https://www. britannica. com/science. *Geophone (accessed on 10 March 2021)*, 2021.

[37] RG Mani and K Von Klitzing. Hall effect under null current conditions. *Applied physics letters*, 64(10):1262–1264, 1994.

[38] Andr Thess, Evgeny V Votyakov, and Yurii Kolesnikov. Lorentz force velocimetry. *Physical Review Letters*, 96(16):164501, 2006.

[39] Michael Stone. *Quantum Hall Effect*. World Scientific, 1992.

[40] Joseph E Avron, Daniel Osadchy, and Ruedi Seiler. A topological look at the quantum hall effect. *Physics today*, 56(8):38–42, 2003.

[41] Liang Fu. *Theory of topological insulators*. PhD thesis, University of Pennsylvania, 2009.

[42] MA Paalanen, DC Tsui, and AC Gossard. Quantized hall effect at low temperatures. *Physical Review B*, 25(8):5566, 1982.

[43] Takashi Oka and Hideo Aoki. Photovoltaic hall effect in graphene. *Physical Review B*, 79(8):081406, 2009.

[44] B Andrei Bernevig and Shou-Cheng Zhang. Quantum spin hall effect. *Physical review letters*, 96(10):106802, 2006.

[45] Markus Konig, Steffen Wiedmann, Christoph Brune, Andreas Roth, Hartmut Buhmann, Laurens W Molenkamp, Xiao-Liang Qi, and Shou-Cheng Zhang. Quantum spin hall insulator state in hgte quantum wells. *Science*, 318(5851):766–770, 2007.

[46] Shuichi Murakami. Phase transition between the quantum spin hall and insulator phases in 3d: emergence of a topological gapless phase. *New Journal of Physics*, 9(9):356, 2007.

[47] Charles Day. Quantum spin hall effect shows up in a quantum well insulator, just as predicted. *Physics Today*, 61(1):19, 2008.

[48] John B Goodenough. Spin-orbit-coupling effects in transition-metal compounds. *Physical Review*, 171(2):466, 1968.

[49] Marcel Franz and Laurens Molenkamp. *Topological Insulators*, volume 6. Elsevier, 2013.

[50] M Zahid Hasan and Charles L Kane. Colloquium: topological insulators. *Reviews of modern physics*, 82(4):3045, 2010.

[51] Desalegne Teweldebrhan and Alexander A Balandin. " graphene-like" exfoliation of atomically-thin films of bi2te3 and related materials: Applications in thermoelectrics and topological insulators. *ECS Transactions*, 33(13):103, 2010.

[52] Ondřej Caha, Adam Dubroka, J Humlicek, V Holy, Hubert Steiner, M Ul-Hassan, Jaime Sanchez-Barriga, Oliver Rader, TN Stanislavchuk, Andrei A Sirenko, et al. Growth, structure, and electronic properties of epitaxial bismuth telluride topological insulator films on baf2 (111) substrates. *Crystal growth & design*, 13(8):3365–3373, 2013.

[53] Phuoc Huu Le and Chih-Wei Luo. Ultrafast dynamics in topological insulators. In *Two-dimensional Materials for Photodetector*. IntechOpen, 2018.

[54] David R Lide. *CRC handbook of chemistry and physics*, volume 85. CRC press, 2004.

[55] M Takaishi. Thermal conductivity measurements of bismuth telluride thin films by using the 3 omega method. *Thermophys Prop*, 27:24–26, 2006.

[56] Bacel Hamdou, Johannes Kimling, August Dorn, Eckhard Pippel, Raimar Rostek, Peter Woias, and Kornelius Nielsch. Thermoelectric characterization of bismuth telluride nanowires, synthesized via catalytic growth and post-annealing. *Advanced Materials*, 25(2):239–244, 2013.

[57] Alka Sharma, TD Senguttuvan, VN Ojha, and Sudhir Husale. Novel synthesis of topological insulator based nanostructures (bi2te3) demonstrating high performance photodetection. *Scientific reports*, 9(1):1–8, 2019.

[58] M Zahid Hasan, Charles L Kane, et al. Topological insulators. *Rev. Mod. Phys*, 82(4):3045–3067, 2010.

[59] Yoichi Ando. Topological insulator materials. *Journal of the Physical Society of Japan*, 82(10):102001, 2013.

[60] Joel E Moore. The birth of topological insulators. *Nature*, 464(7286):194, 2010.

[61] Desalegne Teweldebrhan, Vivek Goyal, and Alexander A Balandin. Exfoliation and characterization of bismuth telluride atomic quintuples and quasi-two-dimensional crystals. *Nano letters*, 10(4):1209–1218, 2010.

[62] RB Mallinson, JA Rayne, and RW Ure Jr. de haas-van alphen effect in n-type bi 2 te 3. *Physical Review*, 175(3):1049, 1968.

[63] S Biswas and R Bhattacharya. Two valence subbands in single crystals of bismuth telluride doped with lead and its electrical properties. *physica status solidi (b)*, 151(1):193–201, 1989.

[64] GE Shoemake, JA Rayne, and RW Ure Jr. Specific heat of n-and p-type bi 2 te 3 from 1.4 to 90 k. *Physical Review*, 185(3):1046, 1969.

[65] Siyuan Zhu, Yukiaki Ishida, Kenta Kuroda, Kazuki Sumida, Mao Ye, Jiajia Wang, Hong Pan, Masaki Taniguchi, Shan Qiao, Shik Shin, et al. Ultrafast electron dynamics at the dirac node of the topological insulator sb 2 te 3. *Scientific reports*, 5(1):1–6, 2015.

[66] Phuoc Huu Le, Po-Tsun Liu, Chih Wei Luo, Jiunn-Yuan Lin, and Kaung Hsiung Wu. Thickness-dependent magnetotransport properties and terahertz response of topological insulator bi2te3 thin films. *Journal of Alloys and Compounds*, 692:972–979, 2017.

[67] Celso I Fornari, Paulo HO Rappl, Sérgio L Morelhão, and Eduardo Abramof. Structural properties of bi2te3 topological insulator thin films grown by molecular beam epitaxy on (111) baf2 substrates. *Journal of Applied Physics*, 119(16):165303, 2016.

[68] Yaguo Wang, Liang Guo, Xianfan Xu, Jonathan Pierce, and Rama Venkatasubramanian. Origin of coherent phonons in bi 2 te 3 excited by ultrafast laser pulses. *Physical Review B*, 88(6):064307, 2013.

[69] AHMED MOOSA and MAYYADAH ABED. Graphene preparation and graphite exfoliation. *Turkish journal of Chemistry*, 45(3):493–519, 2021.

[70] Yeonbae Lee, Chao Ping Liu, Kin Man Yu, and Wladek Walukiewicz. Engineering electronic band structure of indium-doped cd1- xmgxo alloys for solar power conversion applications. *Energy Technology*, 6(1):122–126, 2018.

[71] Daichi Oka, Yasushi Hirose, Masanori Kaneko, Shoichiro Nakao, Tomoteru Fukumura, Koichi Yamashita, and Tetsuya Hasegawa. Anion-substitution-induced nonrigid variation of band structure in srnbo3–x n x (0 x 1) epitaxial thin films. *ACS applied materials & interfaces*, 10(41):35008–35015, 2018.

[72] Tal Heilpern, Manoj Manjare, Alexander O Govorov, Gary P Wiederrecht, Stephen K Gray, and Hayk Harutyunyan. Determination of hot carrier energy distributions from inversion of ultrafast pump-probe reflectivity measurements. *Nature communications*, 9(1):1–6, 2018.

[73] Jean-Claude Diels and Wolfgang Rudolph. *Ultrashort laser pulse phenomena*. Elsevier, 2006.

[74] Orazio Svelto. Solid-state, dye, and semiconductor lasers. In *Principles of Lasers*, pages 365–418. Springer, 1998.

[75] WR Rapoport and Chandra P Khattak. Titanium sapphire laser characteristics. *Applied optics*, 27(13):2677–2684, 1988.

[76] Herman A Haus. Mode-locking of lasers. *IEEE Journal of Selected Topics in Quantum Electronics*, 6(6):1173–1185, 2000.

[77] Jonghan Jin. Dimensional metrology using the optical comb of a mode-locked laser. *Measurement Science and Technology*, 27(2):022001, 2015.

[78] DC Hanna, B Luther-Davies, and RC Smith. Active q switching technique for producing high laser power in a single longitudinal mode. *Electronics Letters*, 15(8):369–370, 1972.

[79] Rihan Wu. *Ultrafast carrier dynamics of porous silicon and gold-silicon composites*. PhD thesis, University of Birmingham, 2021.

[80] Xingyu Zhang, Shengzhi Zhao, Qingpu Wang, Qidi Zhang, Lianke Sun, and Shaojun Zhang. Optimization of cr/sup 4+/-doped saturable-absorber q-switched lasers. *IEEE Journal of Quantum Electronics*, 33(12):2286–2294, 1997.

[81] Giulio Cerullo and Sandro De Silvestri. Ultrafast optical parametric amplifiers. *Review of scientific instruments*, 74(1):1–18, 2003.

[82] Cristian Manzoni and Giulio Cerullo. Design criteria for ultrafast optical parametric amplifiers. *Journal of Optics*, 18(10):103501, 2016.

[83] Nicolas Piro, Felix Rohde, Carsten Schuck, Marc Almendros, Jan Huwer, Joyee Ghosh, Albrecht Haase, Markus Hennrich, Francois Dubin, and Jürgen Eschner. Heralded single-photon absorption by a single atom. *Nature Physics*, 7(1):17–20, 2011.

[84] Vaidya Nathan, Arthur H Guenther, and Shashanka S Mitra. Review of multiphoton absorption in crystalline solids. *JOSA B*, 2(2):294–316, 1985.

[85] Thomas P Pearsall, Federico Capasso, Robert E Nahory, Martin A Pollack, and James R Chelikowsky. The band structure dependence of impact ionization by hot carriers in semiconductors: Gaas. *Solid-State Electronics*, 21(1):297–302, 1978.

[86] Alfred Leitenstorfer and Alfred Laubereau. Ultrafast electronphonon interactions in semiconductors: Quantum kinetic memory effects. In *Semiconductors and Semimetals*, volume 67, pages 1–37. Elsevier, 2001.

[87] JL Oudar, D Hulin, A Migus, A Antonetti, and F Alexandre. Subpicosecond spectral hole burning due to nonthermalized photoexcited carriers in gaas. *Physical review letters*, 55(19):2074, 1985.

[88] Thomas Elsaesser, Jagdeep Shah, Lucio Rota, and Paolo Lugli. Initial thermalization of photoexcited carriers in gaas studied by femtosecond luminescence spectroscopy. *Physical review letters*, 66(13):1757, 1991.

[89] Mark Lundstrom. *Fundamentals of carrier transport*, volume 10. Addison-Wesley Reading, MA, 1990.

[90] Jagdeep Shah. *Ultrafast spectroscopy of semiconductors and semiconductor nanostructures*, volume 115. Springer Science & Business Media, 2013.

[91] PC Becker, HL Fragnito, CH Brito Cruz, J Shah, RL Fork, JE Cunningham, JE Henry, and CV Shank. Femtosecond intervalley scattering in gaas. *Applied physics letters*, 53(21):2089–2090, 1988.

[92] DW Bailey, CJ Stanton, K Hess, MJ LaGasse, RW Schoenlein, and JG Fujimoto. Femtosecond studies of intervalley scattering in gaas and alxga1-xas. *Solid-state electronics*, 32(12):1491–1495, 1989.

[93] W-Z Lin, Robert W Schoenlein, James G Fujimoto, and EP Ippen. Femtosecond absorption saturation studies of hot carriers in gaas and algaas. *IEEE journal of quantum electronics*, 24(2):267–275, 1988.

[94] Robert K Willardson, Eicke R Weber, and Kong-Thon Tsen. *Ultrafast physical processes in semiconductors*. Elsevier, 2000.

[95] U Strauss, WW Rühle, and K Köhler. Auger recombination in intrinsic gaas. *Applied Physics Letters*, 62(1):55–57, 1993.

[96] Jie Zhao, Zhongjie Xu, Yunyi Zang, Yan Gong, Xin Zheng, Ke He, Tian Jiang, et al. Thickness-dependent carrier and phonon dynamics of topological insulator bi 2 te 3 thin films. *Optics Express*, 25(13):14635–14643, 2017.

[97] J Qi, X Chen, W Yu, P Cadden-Zimansky, D Smirnov, NH Tolk, I Miotkowski, H Cao, YP Chen, Y Wu, et al. Ultrafast carrier and phonon dynamics in bi 2 se 3 crystals. *Applied Physics Letters*, 97(18):182102, 2010.

[98] Tian Jiang, Runlin Miao, Jie Zhao, Zhongjie Xu, Tong Zhou, Ke Wei, Jie You, Xin Zheng, Zhenyu Wang, et al. Electron–phonon coupling in topological insulator bi 2 se 3 thin films with different substrates. *Chinese Optics Letters*, 17(2):020005, 2019.

[99] Yuri D Glinka, Sercan Babakiray, Trent A Johnson, Mikel B Holcomb, and David Lederman. Effect of carrier recombination on ultrafast carrier dynamics in thin films of the topological insulator bi2se3. *Applied Physics Letters*, 105(17):171905, 2014.

[100] Hiroyuki Fujiwara. *Spectroscopic ellipsometry: principles and applications*. John Wiley & Sons, 2007.

[101] Jonathan A Sobota, Shuolong Yang, James G Analytis, YL Chen, Ian R Fisher, Patrick S Kirchmann, and Z-X Shen. Ultrafast optical excitation of a persistent surface-state population in the topological insulator bi 2 se 3. *Physical review letters*, 108(11):117403, 2012.

[102] Kazuki Sumida, Y Ishida, S Zhu, Mao Ye, Anna Pertsova, Christopher Triola, Konstantin A Kokh, Oleg E Tereshchenko, Alexander V Balatsky, Shik Shin, et al. Prolonged duration of nonequilibrated dirac fermions in neutral topological insulators. *Scientific reports*, 7(1):1–7, 2017.

[103] Rogier HM Groeneveld, Rudolf Sprik, and Ad Lagendijk. Femtosecond spectroscopy of electron-electron and electron-phonon energy relaxation in ag and au. *Physical Review B*, 51(17):11433, 1995.

[104] RD Averitt and AJ Taylor. Ultrafast optical and far-infrared quasiparticle dynamics in correlated electron materials. *Journal of Physics: Condensed Matter*, 14(50):R1357, 2002.

[105] Jesper Jung, Jakob Bork, Tobias Holmgaard, Niels Anker Kortbek, and K Pedersen. Ellipsometry. *Scientific Project*, pages 1–132, 2004.

[106] RMA Azzam, PG Rigby, and JA Krueger. Kinetics of protein adsorption and immunological reactions at a liquid/solid interface by ellipsometry. *Physics in Medicine & Biology*, 22(3):422, 1977.

[107] Gang Jin, Roger Jansson, and Hans Arwin. Imaging ellipsometry revisited: developments for visualization of thin transparent layers on silicon substrates. *Review of scientific instruments*, 67(8):2930–2936, 1996.

[108] Daisuke Tanooka, Eiki Adachi, and Kuniaki Nagayama. Color-imaging ellipsometer: high-speed characterization of in-plane distribution of film thickness at nano-scale. *Japanese Journal of Applied Physics*, 40(2R):877, 2001.

[109] Qiwen Zhan and James R Leger. High-resolution imaging ellipsometer. *Applied optics*, 41(22):4443–4450, 2002.

[110] Wolfgang Budde. Photoelectric analysis of polarized light. *Applied Optics*, 1(3):201–205, 1962.

[111] Bernhard O Seraphin. Optical properties of solids new developments. 1976.

[112] PS Hauge. Recent developments in instrumentation in ellipsometry. *Surface Science*, 96(1-3):108–140, 1980.

[113] M Kildemo, S Deniau, Pavel Bulkin, and Bernard Drévillon. Real time control of the growth of silicon alloy multilayers by multiwavelength ellipsometry. *Thin Solid Films*, 290:46–50, 1996.

[114] Ilsin An, YM Li, HV Nguyen, and RW Collins. Spectroscopic ellipsometry on the millisecond time scale for real-time investigations of thin-film and surface phenomena. *Review of scientific instruments*, 63(8):3842–3848, 1992.

[115] RW Collins, Joohyun Koh, H Fujiwara, PI Rovira, AS Ferlauto, JA Zapien, CR Wronski, and R Messier. Recent progress in thin film growth analysis by multichannel spectroscopic ellipsometry. *Applied surface science*, 154:217–228, 2000.

[116] PS Hauge and FH Dill. A rotating-compensator fourier ellipsometer. *Optics Communications*, 14(4):431–437, 1975.

[117] A Röseler. Spectroscopic ellipsometry in the infrared. *Infrared Physics*, 21(6):349–355, 1981.

[118] A Röseler and W Molgedey. Improvement in accuracy of spectroscopic ir ellipsometry by the use of ir retarders. *Infrared physics*, 24(1):1–5, 1984.

[119] F Ferrieu. Infrared spectroscopic ellipsometry using a fourier transform infrared spectrometer: Some applications in thin-film characterization. *Review of scientific instruments*, 60(10):3212–3216, 1989.

[120] Kunie Ishioka, Masahiro Kitajima, Oleg V Misochko, and Tadaaki Nagao. Ultrafast phonon dynamics of epitaxial atomic layers of bi on si (111). *Physical Review B*, 91(12):125431, 2015.

[121] AA Melnikov, KN Boldyrev, Yu G Selivanov, VP Martovitskii, SV Chekalin, and EA Ryabov. Coherent phonons in a bi 2 se 3 film generated by an intense single-cycle thz pulse. *Physical Review B*, 97(21):214304, 2018.

[122] Mostafa Keshavarz Moazzam and Hassan Kaatuzian. Electro-plasmonic modal power shifting in metal/insulator/semiconductor structure tailored as a cmos-compatible plasmonic waveguide. *Plasmonics*, 13(4):1373–1385, 2018.